

## Evaluation of the TE<sub>12</sub> mode in circular waveguide for low-loss, high-power rf transmission

Sami G. Tantawi, C.D. Nantista, G.B. Bowden, K.S. Fant, N.M. Kroll, and A.E. Vlieks  
Stanford Linear Accelerator Center, P.O. Box 4349, Stanford, California 94309

Y.-H. Chin, H. Hayano, and V.F. Vogel  
KEK, 1-1 Oho, Tsukuba-shi, Ibaraki-ken 305, Japan

J. Nielson  
Calabazas Creek Research, Inc., 20937 Comer Drive, Saratoga, California 95070  
(Received 12 January 2000; published 3 August 2000)

The use of TE<sub>12</sub> in circular waveguide with smooth walls was suggested for low-loss transport of rf signals in multimoded systems [S.G. Tantawi *et al.*, in *Advanced Accelerator Concepts: Eighth Workshop*, edited by Wes Lawson, AIP Conf. Proc. No. 472 (AIP, New York, 1999), pp. 967–974]. Such systems use the same waveguide to transport different signals over different modes. In this report we detail a series of experiments designed to measure the characteristics of this mode. We also describe the different techniques used to generate it and receive it. The experiments were done at X band around a frequency of 11.424 GHz, the frequency of choice for future linear colliders at X band [The NLC Design Group, Report No. LBNL-PUB-5424, SLAC Report No. 474, Report No. UCRL-ID 124161, 1996; The JLC Design Group, KEK-REPORT-97-1, 1997]. The transportation medium is 55 m of highly over-moded circular waveguide. The design of the joining flanges is also presented.

PACS numbers: 84.40.Az

### I. INTRODUCTION

The high-power rf pulse compression techniques suggested for future linear colliders involves long runs of low loss transportation lines [1–6]. These runs total from 240 to 1000 km depending on the system. They are supposed to carry rf pulses with power levels up to 600 MW for 1.5  $\mu$ s at 11.424 GHz [7]. These transport lines were envisioned to be circular waveguides with smooth walls using the low-loss TE<sub>01</sub> mode. Several experimental pulse compression systems based on such lines were built and operated at power levels up to 500 MW [8,9]. The use of the HE<sub>11</sub> mode in corrugated guide was deemed impractical because the corrugation depth required at X band is large, making the cost of the waveguide high.

To reduce the total length of waveguide and, consequently, the cost, a multimoded rf system was suggested [1]. The reduction in cost using this technique was analyzed and shown to be considerable [7]. This system multiplexes several rf signals inside a single waveguide using different modes. Since these waveguides are used to delay the rf signal, the quantity of interest is the attenuation per unit time for different modes. Figure 1 shows the normalized attenuation coefficient per unit time as a function of the normalized waveguide diameter. In this figure, the normalized waveguide diameter  $\bar{D} = D/\lambda$ , where  $\lambda$  is the wavelength, and the attenuation coefficient is normalized according to

$$\bar{\alpha} = \alpha [\text{Np/s}] \bigg/ f \frac{R_m}{Z_0}, \quad (1)$$

where  $R_m$  is the surface resistance,  $Z_0$  is the free space wave impedance, and  $f$  is the frequency. The modes of

choice are the low-loss TE<sub>01</sub> and the two polarizations of the TE<sub>12</sub> mode. In this report, we study the technical aspects of using the TE<sub>12</sub> mode.

For the generation of the TE<sub>12</sub> mode, a novel mode transducer was developed. This transducer was characterized using a *mode analyzer*, and its transfer characteristics were measured by placing two back-to-back. As the mode

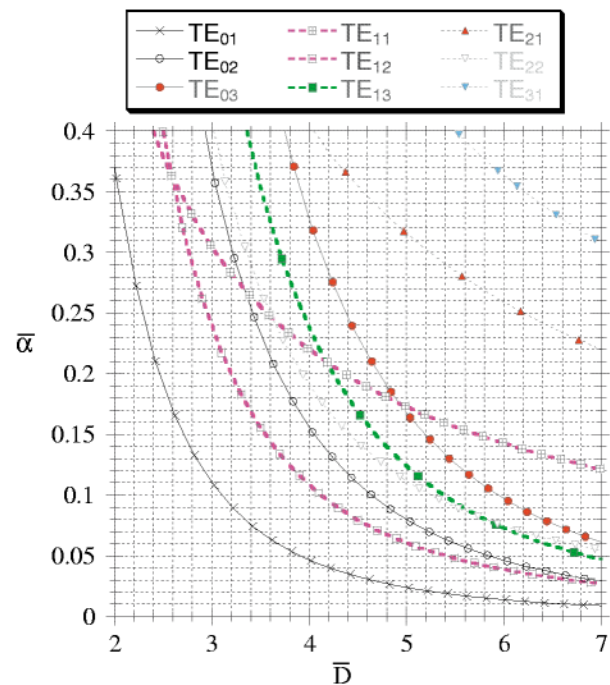


FIG. 1. (Color) Relative attenuation of different TE modes per unit time in circular waveguide versus the normalized diameter of the waveguide.

transducer ends at a diameter smaller than the transport waveguide diameter, special tapers were used to connect between them. We will describe these tapers and their effect on the system efficiency.

The transport line in our experiment was composed of 11 sections of a circular waveguide with a diameter of 12.065 cm. Each section is 5 m long, for a total length of 55 m. The sections were connected using a choked flange connection. This connection was designed to operate well for both the  $TE_{01}$  mode and the  $TE_{12}$  mode. We will describe this design and the procedures used to install this line. We will report results of the attenuation measurements of this line for both  $TE_{01}$  and  $TE_{12}$  modes. Also, the mode analyzer was installed at the end of the line to measure mode conversion due to this highly overmoded waveguide (102 modes can propagate in this guide at the operating frequency). The results showed no noticeable coupling between the two polarizations of  $TE_{12}$ , but there was some coupling from  $TE_{12}$  to the  $TE_{41}$  mode. A discussion of this result and some estimates of the coupling coefficient between modes are presented. According to our results presented below, mode conversion levels were small, and the overall efficiency of the transport line using the  $TE_{12}$  mode was high and comparable to that of the  $TE_{01}$  mode.

## II. THE MODE ANALYZER AND MEASUREMENT SETUP

### A. The mode analyzer

To understand the effects of transporting rf signals in highly overmoded circular waveguide, we need to quanti-

tatively analyze the modes present in this guide. The idea of the mode analyzer presented here depends on mapping the magnitude and phase of the magnetic field on the walls of the waveguide in both the azimuthal and axial directions. From this map, one can deduce the modes carried by the waveguide. The mapping of the field is accomplished mechanically by measuring a signal through a small circular aperture, which can move in both the azimuthal and axial directions. This is shown in Fig. 2. The system is composed of three different waveguides. The middle one is slightly bigger than the other two; hence, it can slide axially and azimuthally between them. The size of the step discontinuity is 1.905 mm (difference in radius between the middle waveguide and the two outer ones). The outer tubes have the same diameter as the transport line, 12.065 cm. This discontinuity is thus very small compared with the size of the waveguide. A mode matching simulation is shown in Fig. 3. It shows the mode conversion due to this step discontinuity for different incident signals.

The motion of the middle waveguide is controlled by a linear stage on top of which an azimuthal stage is mounted. Each stage is controlled by a stepper motor with a general purpose interface bus (GPIB) interface to a PC. The linear stage controls the motion of the middle waveguide to  $\pm 1 \mu\text{m}$ . The azimuthal stage controls the azimuthal position to  $\pm 1 \text{ mdeg}$ . The middle waveguide has a small coupling aperture, which couples its signal to a rectangular waveguide. The orientation of the rectangular waveguide controls the component of the magnetic field being measured. If the large dimension of the waveguide is parallel

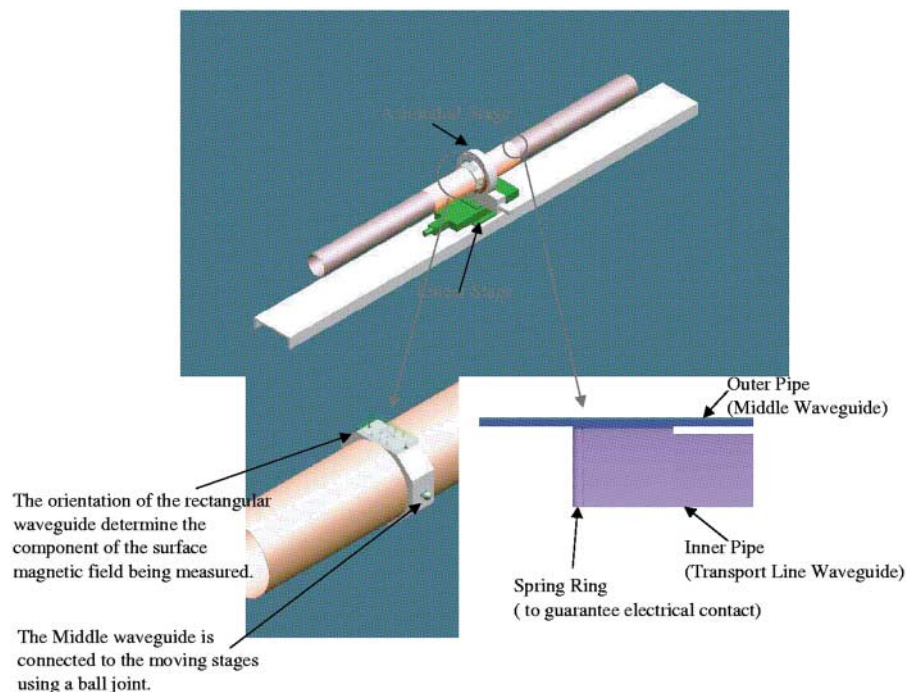


FIG. 2. (Color) The mode analyzer.

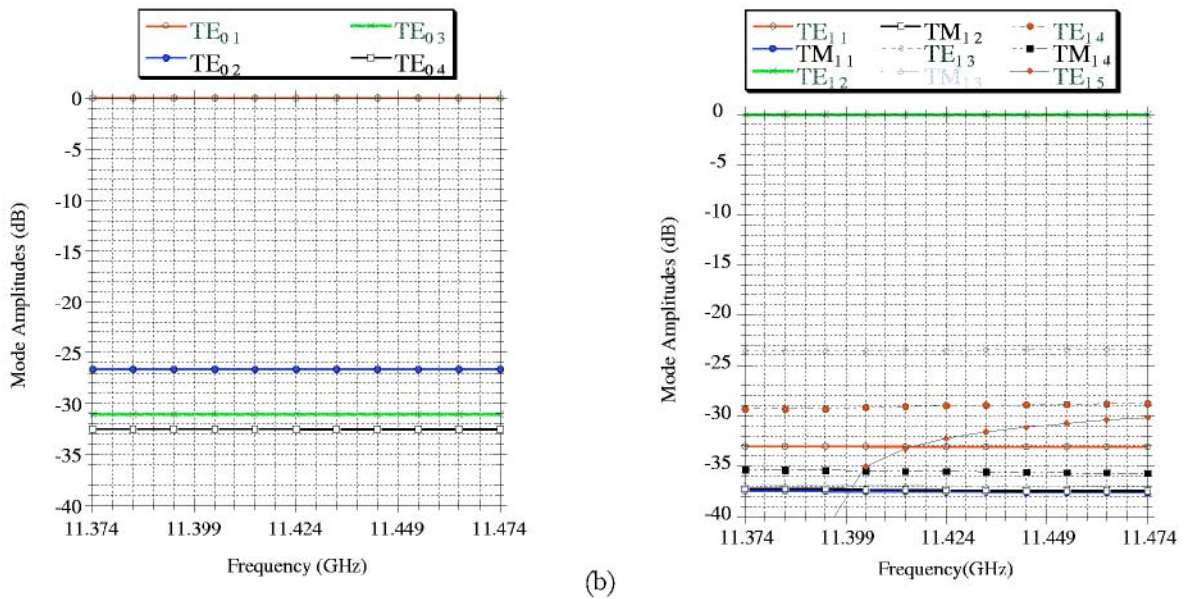


FIG. 3. (Color) (a) The scattering of modes due to the step discontinuity when the incident mode is the TE<sub>01</sub> mode. (b) The scattering of modes due to the step discontinuity when the incident mode is the TE<sub>12</sub> mode.

to the circular waveguide axis, the axial magnetic field is being measured; if the large dimension of the waveguide is perpendicular to the axis of the circular guide, the azimuthal magnetic field is being measured. The orientation of the rectangular guide is fixed to an accuracy of 1 mdeg.

To measure the signal from the coupling aperture while the system is in motion a phase and amplitude stable coaxial cable is used. This cable is connected to the waveguide using a broadband calibrated waveguide to coaxial adapter. The coaxial cable is a 1.5 m long Gore cable [10].

### B. The measurement setup

A typical measurement setup is shown in Fig. 4. In all measurements, an HP 8510C network analyzer was used. The signal generated by the sweep oscillator is first fed to a high-power amplifier, then split using a 20 dB directional coupler. The low-level signal output of the directional coupler feeds the S-parameter test set (HP 8515A). The high-power signal of the directional coupler is fed to a 55 m rectangular waveguide, which feeds a mode launcher at the beginning of the transport line. At the end of the transport line

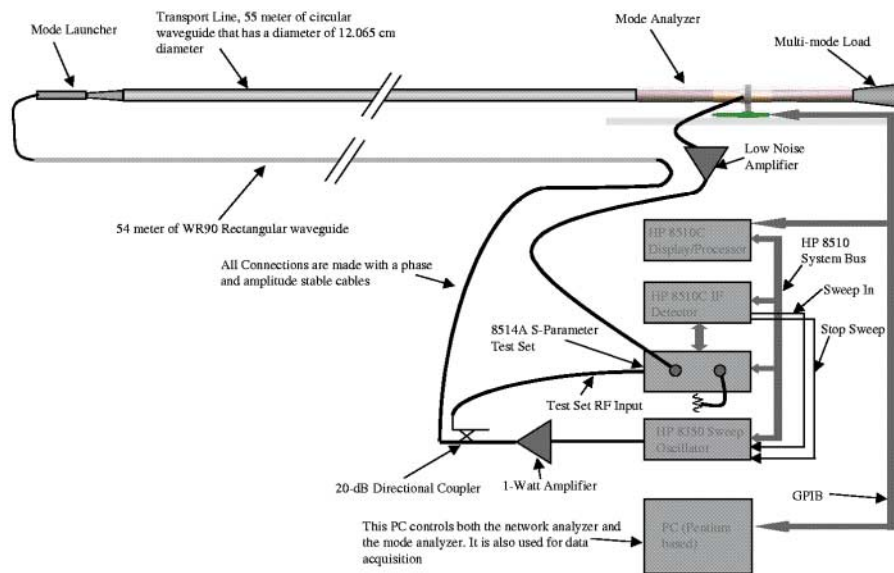


FIG. 4. (Color) Typical measurement setup.

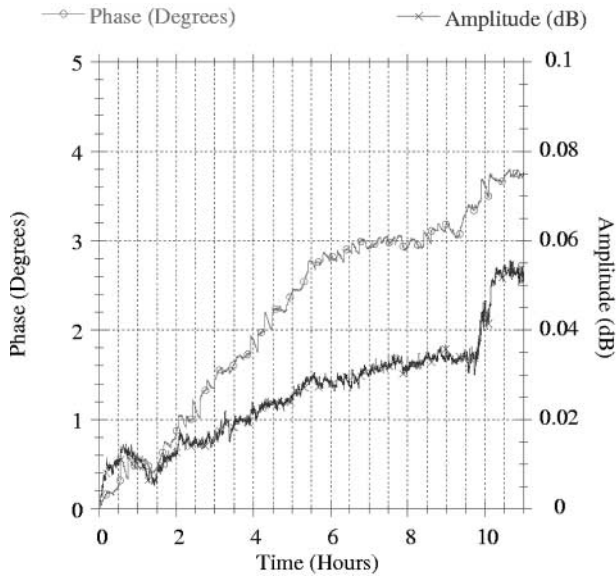


FIG. 5. Stability of measurements over time.

line, the mode mapper is installed. The signal from the mode analyzer is fed to a low noise linear amplifier (noise figure = 3 dB). The output of the low noise amplifier is fed back to the  $S$ -parameter test setup. The network analyzer measurements and the mode mapper movements are controlled with a single PC, using a GPIB link and a software program written in Lab View [11].

To map the field over the surface of the waveguide, the number of measurements is typically 3000 points. This takes up to two hours, because of the time needed by the mechanical movements and the data acquisition system. Phase changes due to temperature variation could affect these measurements because of the long runs of waveguides ( $\sim 115$  m of waveguide). To ensure that this would not be a factor, the ATF tunnel [12] was chosen as the experimental site. The circular waveguide was installed on top of the ATF linac. The temperature of this tunnel is controlled to within  $\pm 0.5$  °C. A measurement of the change in phase and amplitude over the whole length of the 115 m of waveguide at 11.424 GHz is shown in Fig. 5. These measurements include all the amplifiers and network analyzer. The period of these measurements is 11 h. Clearly, the stability of the system over the 2 h period, which is required to map the field, is quite good.

The mode analyzer is terminated by a radiating horn. This horn is padded with lossy material. The idea here is to create, as much as possible, a matched load for all modes.

### C. Interpretation of the measured data

Although the system is rigged to measure both axial magnetic field  $H_z$  and azimuthal magnetic field  $H_\phi$ , for expediency we measured only  $H_z$ . This field exists only in TE modes. Hence, all our measurements were for the TE modes only, which simplified the data analysis. Coupling to TM modes was expected to be negligible for small, gradually changing wall imperfections.

The data, which are a function of the angle  $\phi$  and the axial position  $z$ , are measured at discrete positions, i.e.,  $H_z = H_z(m\delta\phi, n\delta z)$ , where  $m$  and  $n$  are integers and  $\delta\phi = \frac{2\pi}{m}$  and  $\delta z = \frac{S}{I-1}$  are the spacing between measurements in both the  $\phi$  and  $z$  directions, respectively. The number of points in the azimuth is  $M$ . The number of points in the axial direction is  $I$ , which is measured over a span  $S$ . These data are the result of the field induced by all possible TE modes in the middle guide, i.e.,

$$H_z(m\delta\phi, i\delta z) = \sum_{n=-N}^{n=+N} \sum_{l=1}^{L(n)} h_{z^-}^{n,l} e^{jnm\delta\phi + jk_{nl}i\delta z} + h_{z^+}^{n,l} e^{jnm\delta\phi - jk_{nl}i\delta z}, \quad (2)$$

where  $h_{z^+}^{n,l}$  and  $h_{z^-}^{n,l}$  are the field components of the forward and backward propagating  $TE_{nl}$  mode, respectively, and  $k_{nl}$  is the propagation constant of that mode. When  $n$  is positive, the mode is right-hand circularly polarized when it propagates in the forward direction and left-hand circularly polarized when it propagates in the backward direction, and vice versa for negative  $n$ . The summation is taken over all possible propagation modes in this waveguide, that is,  $N$  is the highest azimuthal number for a mode that can propagate in this guide, and  $L(n)$  is the number of modes that can propagate with azimuthal index  $n$ .

The first step in analyzing this data is to multiply Eq. (2) by  $e^{-jn'm\delta\phi}$  and perform a summation over  $m$  to get

$$\begin{aligned} \hat{H}_z(n', i\delta z) &= \sum_{m=1}^M H_z\left(m\frac{2\pi}{M}, i\delta z\right) e^{-jn'm(2\pi/M)} \\ &= M \sum_{l=1}^{L(n')} h_{z^-}^{n',l} e^{jk_{n'l}i\delta z} + h_{z^+}^{n',l} e^{-jk_{n'l}i\delta z}. \end{aligned} \quad (3)$$

The Fourier components  $\hat{H}_z(n', i\delta z)$  contain only information about  $TE_{n'l}$  modes. For a given azimuthal number  $n'$ , a set of linear equations is constructed by multiplying Eq. (3) by  $e^{\pm jk_{n'l}i[S/(I-1)]}$  and performing a summation over  $i$ , for all possible  $l'$ , to get

$$\begin{aligned} \sum_{i=0}^{I-1} \hat{H}_z\left(n', i\frac{S}{I-1}\right) e^{jk_{n'l'}i[S/(I-1)]} &= M \sum_{l=1}^{L(n')} \left[ h_{z^-}^{n',l} \frac{\sin\left[\frac{I}{I-1}(k_{n'l} + k_{n'l'})\frac{S}{2}\right]}{\sin\left[\frac{1}{I-1}(k_{n'l} + k_{n'l'})\frac{S}{2}\right]} e^{j(k_{n'l} + k_{n'l'})S/2} \right. \\ &\quad \left. + h_{z^+}^{n',l} \frac{\sin\left[\frac{I}{I-1}(-k_{n'l} + k_{n'l'})\frac{S}{2}\right]}{\sin\left[\frac{1}{I-1}(-k_{n'l} + k_{n'l'})\frac{S}{2}\right]} e^{j(-k_{n'l} + k_{n'l'})S/2} \right], \end{aligned} \quad (4a)$$

$$\sum_{i=0}^{I-1} \hat{H}_z \left( n', i \frac{S}{I-1} \right) e^{-jk_{n'l}i[S/(I-1)]} = M \sum_{l=1}^{L(n')} \left[ h_z^{n',l} \frac{\sin[\frac{I}{I-1} (k_{n'l} - k_{n'l'}) \frac{S}{2}]}{\sin[\frac{1}{I-1} (k_{n'l} - k_{n'l'}) \frac{S}{2}]} e^{j(k_{n'l} + k_{n'l'})S/2} + h_z^{n',l} \frac{\sin[\frac{I}{I-1} (-k_{n'l} - k_{n'l'}) \frac{S}{2}]}{\sin[\frac{1}{I-1} (-k_{n'l} - k_{n'l'}) \frac{S}{2}]} e^{j(-k_{n'l} + k_{n'l'})S/2} \right]. \quad (4b)$$

Equations (4a) and (4b) represent a set of  $2L(n')$  linear equations for the  $2L(n')$  unknowns,  $h_z^{n',l}$ . Solving these equations yields the field component due to each mode. These field components are related to the power  $P_{nl}$  carried by the modes by

$$P_{nl} \propto \frac{k_{nl}}{kc_{nl}^4} (kc_{nl}^2 a^2 - n^2) (h_z^{n,l})^2, \quad (5)$$

where  $kc_{nl}$  is the cutoff wave number of the TE<sub>*nl*</sub> mode and  $a$  is the radius of the waveguide. Using Eq. (5) one can get the relative level for each mode that propagates in the middle waveguide.

#### D. Calibration of the WR90 waveguide

It is very important to measure accurately the attenuation of the WR90 waveguide, which sends the signal down to the beginning of the transport line, and the stable cable that connects this waveguide to the mode launcher.

To this end, we split this waveguide in half to form a U-shaped waveguide transmission line. The turnaround of this U shape was accomplished using the stable cable mentioned earlier. The resultant attenuation measurement using the HP 8510 network analyzer is shown in Fig. 6.

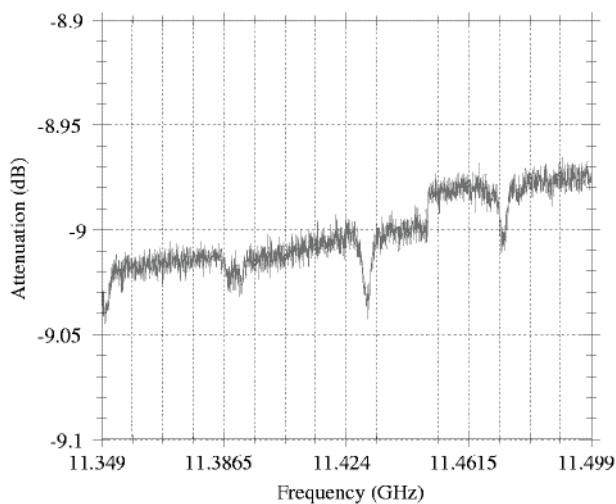


FIG. 6. Rectangular waveguide calibration measurements.

### III. MODE TRANSDUCERS

#### A. Circular-to-rectangular-taper mode transducer

It was observed that a smooth taper from circular to rectangular waveguide preserves the modal structure of both guides [7]. That is, a smooth transition from rectangular to circular waveguide can preserve their common reflection symmetries. The  $S$  matrix of the transition connects modes of the same symmetry class and, for a sufficiently adiabatic transition, preserves their TE (or TM) character. It is then also nonreflecting and, in the absence of degeneracy, its modal connections are one-to-one and order preserving. This property enables us to carry out all of the manipulations in the more easily handled overmoded rectangular waveguide.

In cylindrical coordinates, a shape  $i$  placed with cylindrical symmetry around the  $z$  axis can be described by the relation  $r_i(\phi)$ , which gives the radius as a function of the angle  $\phi$ . The taper between two shapes  $r_1(\phi)$  and  $r_2(\phi)$  is then given by

$$r(\phi, z) = r_1(\phi) + \frac{r_2(\phi) - r_1(\phi)}{l} z, \quad (6)$$

where  $l$  is the length of the taper. This taper is compatible with the process of wire electric discharge machining (EDM) when the two heads of the machine are moving synchronously with the same angular speed. A taper with sufficient length connecting a square waveguide to a

TABLE I. Modal connection between circular and square waveguides.

Circular guide modes	Square guide modes
TE <sub>11</sub> (polarization #1)	TE <sub>10</sub>
TE <sub>11</sub> (polarization #2)	TE <sub>01</sub>
TM <sub>01</sub>	TM <sub>11</sub>
TE <sub>21</sub> (polarization #1)	TE <sub>20</sub> and TE <sub>02</sub> (in phase)
TE <sub>21</sub> (polarization #2)	TE <sub>11</sub>
TE <sub>01</sub>	TE <sub>20</sub> and TE <sub>02</sub> (out of phase by 180°)
TM <sub>11</sub> (polarization #1)	TM <sub>12</sub>
TM <sub>11</sub> (polarization #2)	TM <sub>21</sub>
TE <sub>31</sub> (polarization #1)	TE <sub>12</sub>
TE <sub>31</sub> (polarization #2)	TE <sub>21</sub>
TM <sub>21</sub> (polarization #1)	TM <sub>22</sub>
TM <sub>21</sub> (polarization #2)	TM <sub>13</sub> and TM <sub>13</sub> (in phase)
TE <sub>41</sub> (polarization #1)	TE <sub>22</sub>
TE <sub>41</sub> (polarization #2)	TE <sub>31</sub> and TE <sub>13</sub>
TE <sub>12</sub> (polarization #1)	TE <sub>30</sub>
TE <sub>12</sub> (polarization #1)	TE <sub>03</sub>
TM <sub>02</sub>	TM <sub>31</sub> and TM <sub>13</sub> (out of phase by 180°)

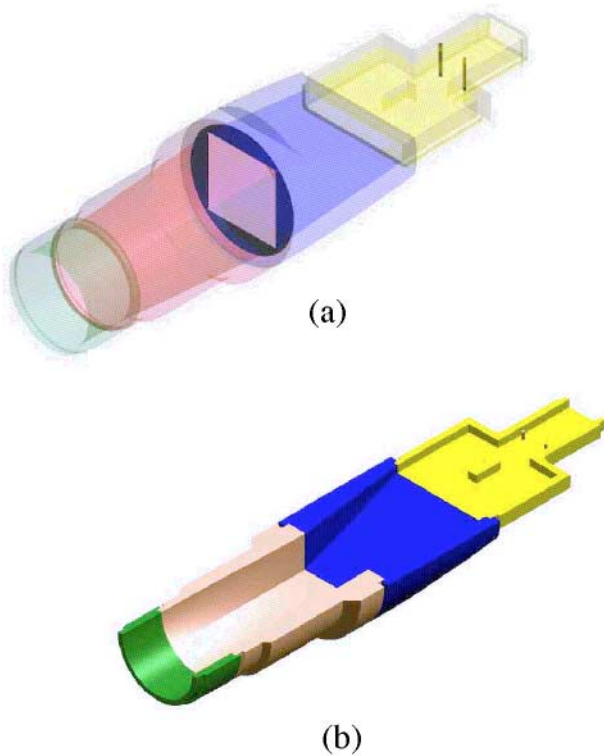


FIG. 7. (Color) (a) The circular-to-rectangular-tapers  $TE_{12}$  mode transducer. (b) A cutaway view of the structure.

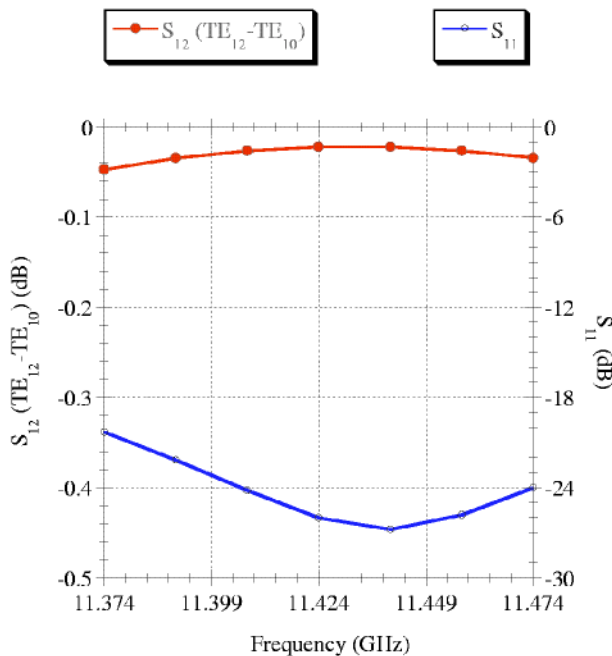


FIG. 8. (Color) Simulated performance of the  $TE_{10}$  (rectangular) to  $TE_{12}$  (circular) mode converter. Simulations were done using HP-HFSS.

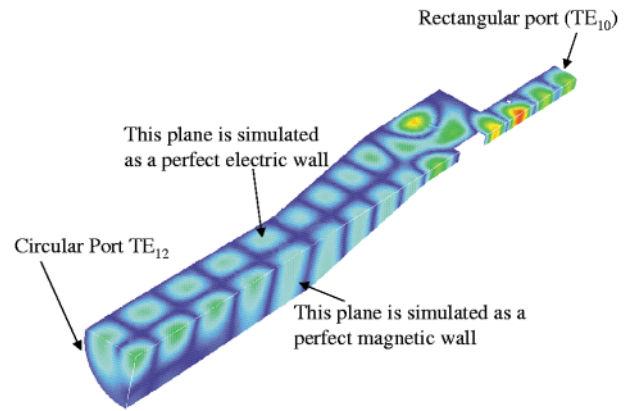


FIG. 9. (Color) Simulated electric field distribution inside the  $TE_{12}$  mode transducer. The colors represent the electric field strength.

circular waveguide would have the modal connection shown in Table I.

It is clear from Table I that the  $TE_{12}$  mode can be generated in circular waveguide by using this type of transition after generating a  $TE_{30}$  mode in a square waveguide. Hence, the structure of the mode transducer shown in Fig. 7. The device is composed of three sections. The first section converts from  $TE_{10}$  in standard size WR90 rectangular waveguide to  $TE_{30}$  in rectangular guide which has the same height as the WR90 guide but with the width of approximately 3 times that of the WR90 guide. The design was made using HP-HFSS [13]. The design philosophy of this part is to start with a sudden jump in width from the standard WR90 guide to a larger width that allows the  $TE_{30}$  to propagate. Because of symmetry, only  $TE_{n0}$

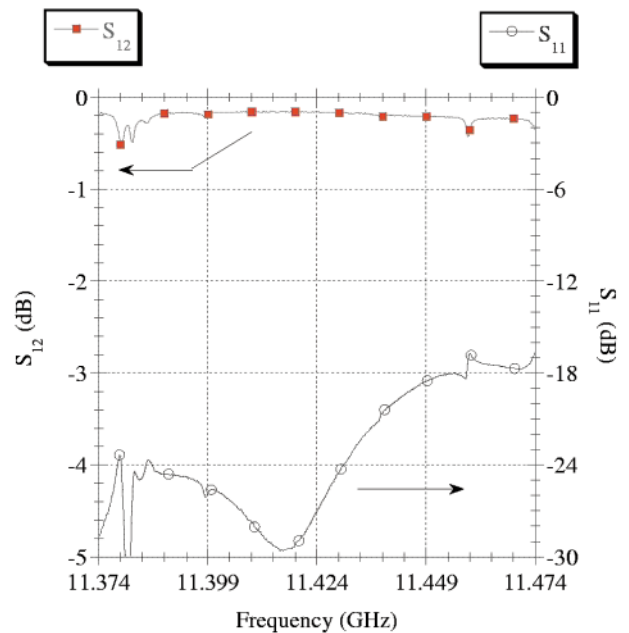


FIG. 10. (Color) Measured frequency response of two  $TE_{12}$  mode transducers connected back-to-back.

modes, with  $n$  being an odd integer, can get excited. If the width is kept small enough so that TE<sub>50</sub> cannot propagate, the only two modes that get excited are TE<sub>10</sub> and TE<sub>30</sub>. A rectangular post is then placed in the middle of the triple-width guide to couple TE<sub>10</sub> and TE<sub>30</sub>. The width, height, and axial location of this post are designed using trial and error until a pure TE<sub>30</sub> mode is obtained. The residual reflection due to all these discontinuities is taken out by the use of two inductive posts placed systemically inside the single-moded WR90 waveguide.

The height of the rectangular guide, which contains the TE<sub>30</sub> mode, is tapered up linearly until the shape of the waveguide becomes a square. The length of this taper is increased until there is no mode conversion to either TE or TM modes. The square waveguide is then tapered to a circular waveguide according to Eq. (1). Again, the length of this taper is increased until the TE<sub>30</sub> mode in the square guide is transformed completely into TE<sub>12</sub> in the circular guide without conversion to any other modes. The overall length of the device is about 23 cm. This is

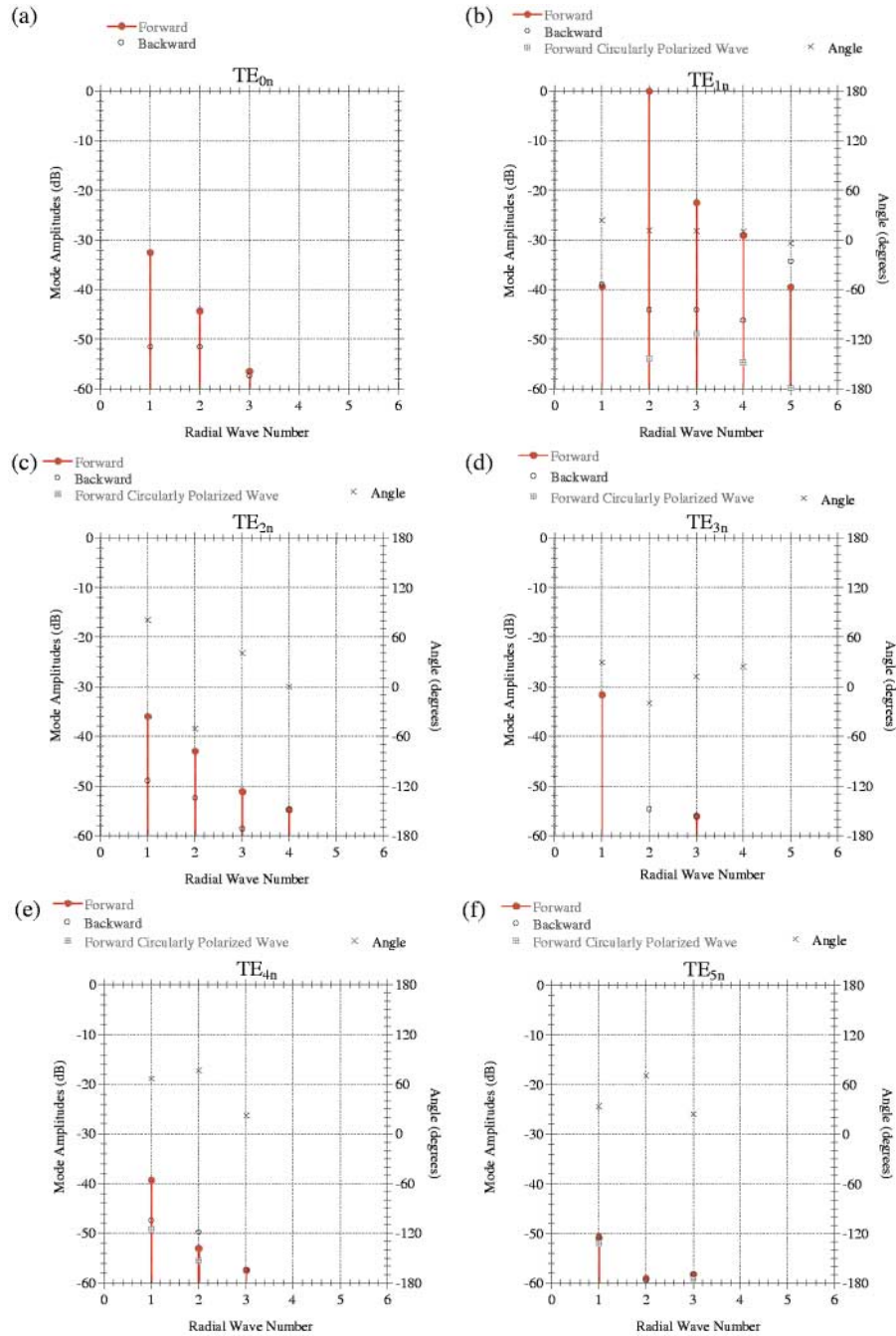


FIG. 11. (Color) Measured mode spectrum of the TE<sub>12</sub> mode transducer. The decomposition is done in terms of a linearly polarized component and a circularly polarized one. The angles in these graphs are the inclination angle of the linearly polarized field component with respect to the vertical direction.

quite compact. Figure 8 shows the simulated frequency response. Figure 9 shows the electric field distribution inside this mode transducer. All simulations were done using the finite-element code HP-HFSS.

To verify the performance, we built two copies of the device and measured them back-to-back. The two mode converters were connected to each other at their circular ports. The measurements were done through the single-moded rectangular ports. The results are shown in Fig. 10. The device performance is good. Nonetheless, the total transmission efficiency is less than simulation prediction. Part of this difference could be attributed to Ohmic losses.

Finally, we measured the modal spectrum of this mode transducer using the mode analyzer described above. To do this measurement, we used the nonlinear taper described in Sec. III E to taper from the mode converter diameter of 5.08 to 12.065 cm, the diameter of the transport line and the input diameter of the mode analyzer. The results are

shown in Fig. 11. The highest level spurious mode is the  $TE_{13}$  mode. This is apparently due to the mode analyzer itself, as the level agrees well with the mode-matching code prediction shown in Fig. 3(b).

### B. The wrap-around mode converter: A $TE_{01}$ mode transducer

A schematic diagram of this mode transducer is shown in Figs. 12(a) and 12(b), and the physical model is shown in Fig. 12(c). The converter is basically composed of a circular waveguide fed from the side by a number of rectangular waveguides. The orientation of these rectangular guides is such that their transverse magnetic field is parallel to the circular waveguide axis. Hence, only TE modes are excited in the circular guide. If the signals from all the rectangular guides are equal in phase and amplitude, the only modes that can get excited in the circular guide are  $TE_{0n}$

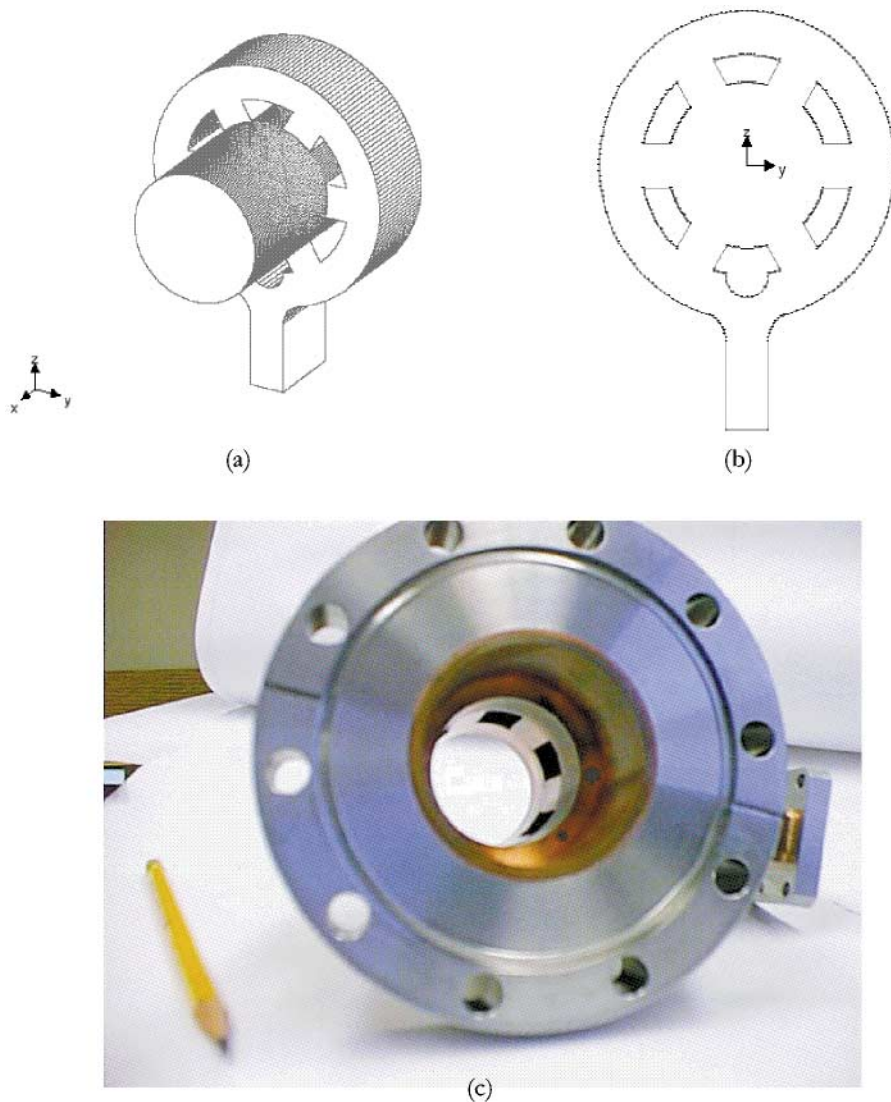


FIG. 12. (Color) The wrap-around mode converter. The physical model shown in the picture does not have the back wall shorting plate. This is done for illustration purposes only.

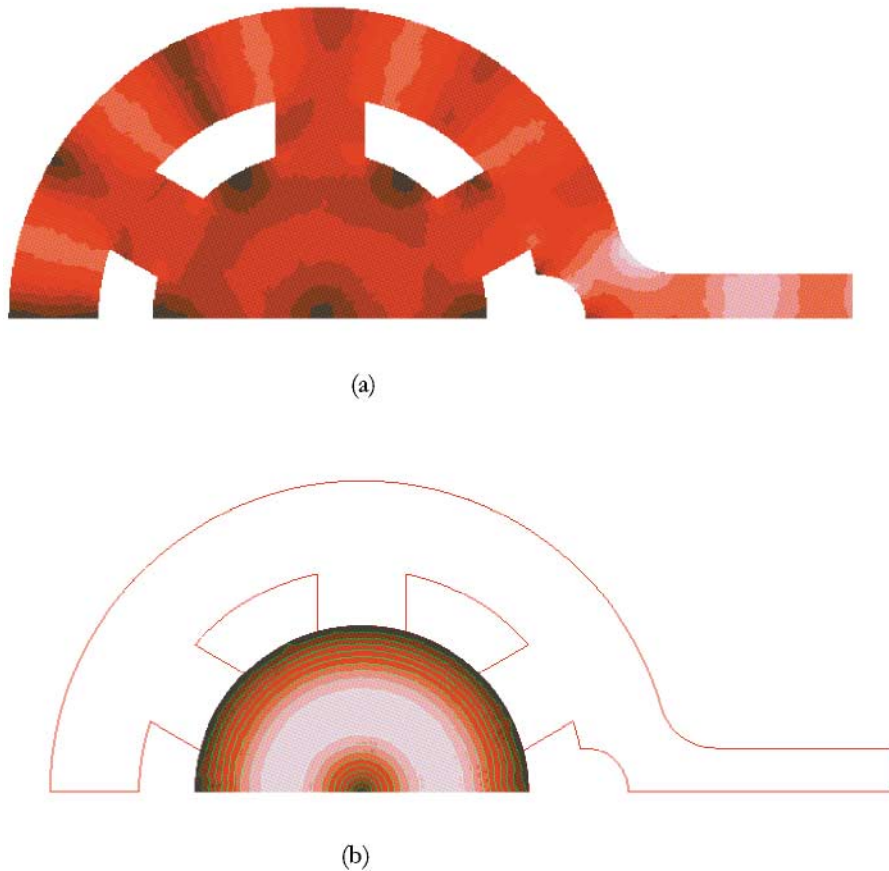


FIG. 13. (Color) HFSS simulation results for the wrap-around converter. The color shades represent the magnitude of the electrical field at (a) a cut plane through the slots and (b) a cut plane in the circular guide 2.5 cm away from the slots.

and TE<sub>*mn*</sub>, where *m* is the number of rectangular waveguides feeding the circular guide or a multiple thereof. The cutoff frequency of the TE<sub>01</sub> mode is greater than the cutoff frequency of the TE<sub>31</sub> mode but smaller than the cutoff frequency of any TE<sub>*m*1</sub> mode, where *m* ≥ 4. Therefore, if the number of rectangular guides is greater than or equal to 4, the circular guide diameter can be chosen such that TE<sub>01</sub> is the only propagating mode that can get excited. In this converter, the number of rectangular waveguides is 6.

To get an equal excitation through the internal coupling rectangular guides, a single, common, rectangular guide feeds them. This guide is wrapped around the device. Because of the geometrical and excitation symmetry around the *zx* plane, only one-half the device need be considered, as shown in Fig. 13(a). From a circuit point of view, the curved rectangular guide should feed the connecting rectangular guides [as shown in Fig. 13(a)] at an interval of  $n\lambda_g$ , where  $\lambda_g$  is the wavelength in the curved guide and *n* is an integer. In this case, *n* = 1. The short circuit at the end of the curved guide, produced by the symmetry plane, should be located  $\lambda_g/4$  away from the last waveguide feed. A bulge splits the power around the symmetry plane at the entrance of the rectangular guide, as shown in Fig. 13(a).

The final design dimensions were carried out using HP-HFSS [5]. The field in a cross section of the circular guide

that contains the feeding rectangular guides is shown in Fig. 13(a). Away from the slot perturbation the field in the circular guide is shown in Fig. 13(b).

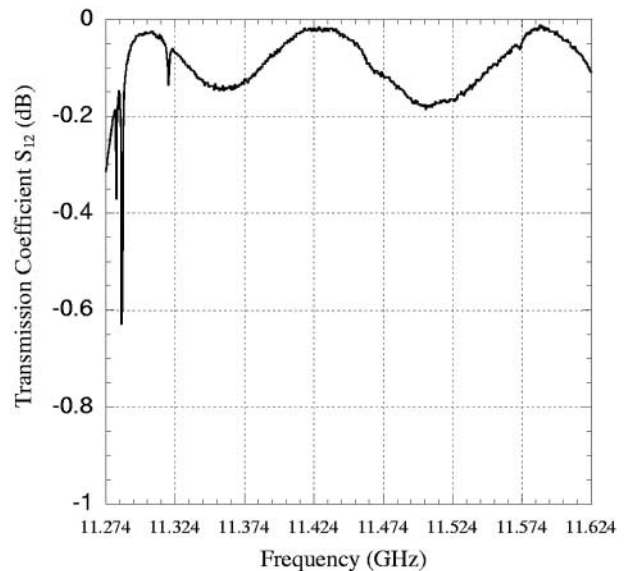


FIG. 14. Measured transmission coefficient for two wrap-around mode converters back-to-back. The device is optimized at 11.424 GHz.

The device, as described, is basically a three-port device: one rectangular input and two circular outputs. One of the design criteria was to achieve the following scattering matrix for the three-port device:

$$S = \begin{pmatrix} -1/3 & 2j/3 & 2j/3 \\ 2j/3 & 1/3 & -2/3 \\ 2j/3 & -2/3 & 1/3 \end{pmatrix}. \quad (7)$$

With this scattering matrix, shorting one of the circular ports would achieve a perfect transmission between the remaining two ports. We could approach this matrix, but not perfectly. The remaining small mismatch after shorting one of the circular ports was a reflection coefficient of 0.21. The device was matched using an iris in the circular waveguide. Figure 14 shows transmission measurements of two mode converters connected back-to-back at their circular ports.

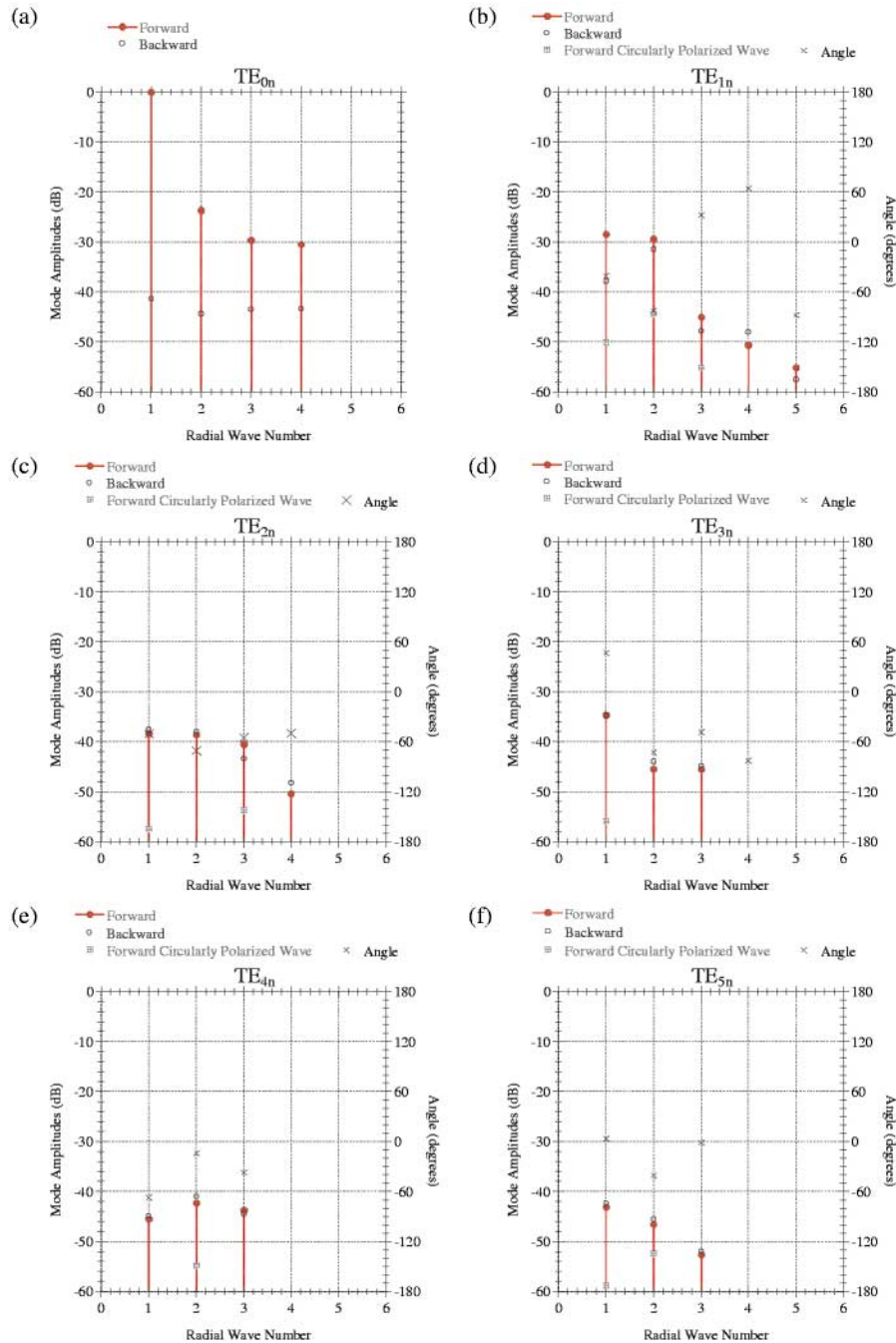


FIG. 15. (Color) Measured mode spectrum of the TE<sub>01</sub> mode transducer. The decomposition is done in terms of a linearly polarized component and a circularly polarized one. The angles in these graphs are the inclination angle of the linearly polarized field component with respect to the vertical direction.

Finally, we measured the mode spectrum of that transducer. This was done with the aid of the nonlinear arc taper described below. It was used to match the diameter of the mode transducer to that of the mode analyzer. The measurements are shown in Fig. 15. The level of the TE<sub>02</sub> mode is slightly higher than that predicted by the mode-matching simulations of the mode analyzer. This could be due to the arc taper. A level as small as -34 dB of TE<sub>02</sub> contamination due to the taper, combined with the TE<sub>02</sub> contamination produced by the mode analyzer, could result in the -23.6 dB TE<sub>02</sub> level observed in the measurements. This is, of course, dependent on the phase between the two sources of contamination. The simulation of the arc taper, reported below, shows that it produces TE<sub>02</sub> with levels up to -25.3 dB.

### C. An arc taper for TE<sub>01</sub> and TE<sub>12</sub>

Both mode converters described in Secs. III A and III B above end up at a diameter of 5.08 cm. A compact taper that connects these mode transducers to the transport line, which has a diameter of 12.065 cm, is needed. The taper profile was optimized for mode purity using a cubic spline fit to selected points at intervals along the wall [14,15]. A cubic spline fit ensured that the resulting wall profile varied smoothly, so as to minimize unwanted reflections. The initial trial shape for optimization was an arc taper. The simulation was done with the procedure described in [15]. The final wall profile is shown in Fig. 16, and the simulated performance is shown in Table II.

To verify the performance of this taper, we used two of them to connect the TE<sub>01</sub> and TE<sub>12</sub> mode transducers. The experimental measurements are shown in Figs. 17 and 18. In comparison with Figs. 10 and 14, one can conclude that the arc tapers are performing well.

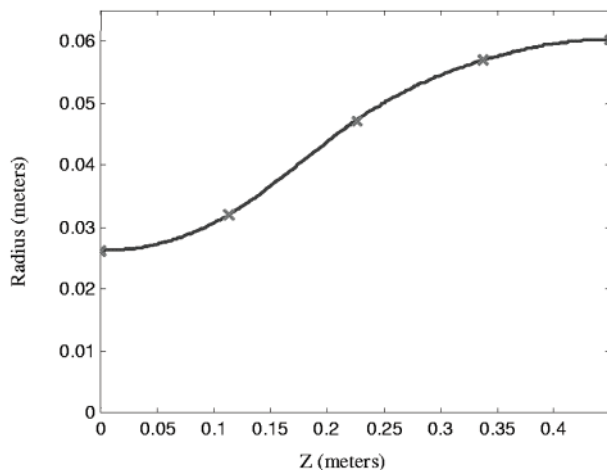


FIG. 16. Arc taper profile.

TABLE II. The simulated response of the arc taper.

Mode output	Power (dB)
TE <sub>12</sub> incident on the small diameter of the taper	
Sum of reflected power:	-30.0 dB
TE <sub>11</sub>	-32.7438
TM <sub>11</sub>	-24.2549
TE <sub>12</sub>	-0.0187
TE <sub>01</sub> incident on the small diameter of the taper	
Sum of reflected power:	-70 dB
TE <sub>01</sub>	-0.0128
TE <sub>02</sub>	-25.3265
TE <sub>03</sub>	-49.1235
TE <sub>04</sub>	-67.0160

### D. Flanges and connections

The electrical continuity of the inner waveguide wall is interrupted by gaps at the flange joints between components and between transport line sections. For the TE<sub>01</sub> mode, such short gaps are inconsequential since the wall currents flow only in the  $\phi$  direction. The TE<sub>12</sub> mode, however, has longitudinal currents as well, so longitudinal discontinuities can cause reflections and couple power into parasitic modes. To provide effective continuity across flange joints, we designed special “choke” flanges. Grooves machined in the flange faces create a resonance at 11.424 GHz between themselves and the gap at the waveguide wall when an electric boundary condition is assumed at the latter position. This provides the proper gap impedance for the waveguide mode. At the same time, it prevents rf from leaking out beyond the groove.

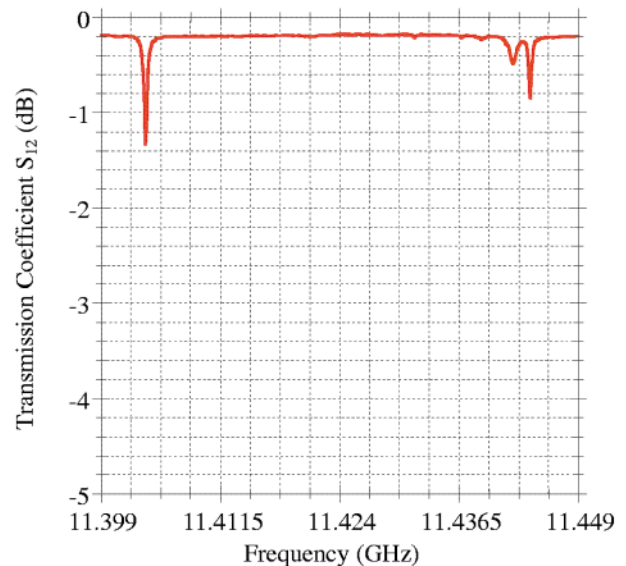


FIG. 17. (Color) The transmission through two TE<sub>12</sub> mode transducers connected from their circular ports using the arc tapers.

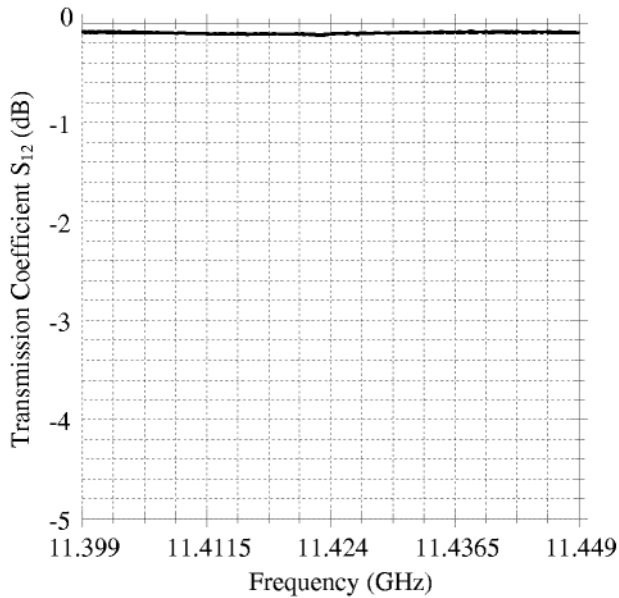


FIG. 18. The transmission through two  $TE_{01}$  mode transducers connected from their circular ports using the arc tapers.

Chokes were designed using MAFIA [16] with  $rz$  geometry and  $n = 1$  azimuthal symmetry. The gap must be cut off for  $TE_{0n}$ -like radial waveguide modes, and thus for any modes with an azimuthal electric field. Therefore, the longitudinal  $H$  field at the wall will not excite gap modes. It is assumed that the azimuthal  $H$  field of the traveling  $TE_{12}$  wave at the wall is approximately constant across the gap opening, since the gap is short compared to the guide wavelength. A standing wave resonance beyond the waveguide wall which matches this field is then sought. The groove creates a resonance insensitive to the exact geometry and electrical contact where the flanges meet at a larger radius. The electric field goes to zero at the gap opening and at the back of the groove and reaches a maximum around the bend from the gap into the groove. The radial position, width, and depth of this groove are adjusted to give this resonance the desired frequency.

Two gap flange designs were used in our experiment. For component connections, we have a 5.08 cm diameter, one-sided choke, for which the opposing flange face must be flat. For 12.065 cm diameter connections, we have a two-sided choke, for which a groove is machined in each flange. The gap widths are 2.34 and 2.03 mm, respectively. The grooves begin at radii 5.00 and 5.18 mm beyond the gap openings, with radial widths of 3.30 and 5.08 mm and depths into the flange faces of 6.55 and 7.62 mm. Figure 19 shows a MAFIA simulation of the larger waveguide two-sided choke cut at the symmetry plane. Note the absence of field beyond the groove.

## E. $TE_{12}$ mode rotator

### 1. Polarization mixing

A potential problem arises with the use of a polarized circular waveguide mode for power transmission. The orthogonal polarizations of the mode are degenerate in wave number, so their relative phase remains fixed as they propagate. This means that extended imperfections or repeated, similar imperfections which couple the modes are not limited in how much power transfer they can cause, as they normally are by the finite beat wavelength of nondegenerate modes.  $TE_{01}$  also has a degenerate mode,  $TM_{11}$ , but the two are coupled by the bending of the guide axis, and any power transfer is undone by a return to the parallel direction.

Cross polarizations of  $TE_{12}$  are coupled by elliptical deformations or, more precisely, by the  $n = 2$  azimuthal Fourier component of the wall displacement. The coupling phenomenon can be understood as the splitting of the wave number degeneracy for polarizations along the major and minor axes of the deformed guide. The projected components along these axes of a wave linearly polarized along another direction get out of phase, resulting in an elliptically polarized wave. To get a quantitative understanding of this danger, we can use perturbation theory to calculate the cutoff wave number splitting.

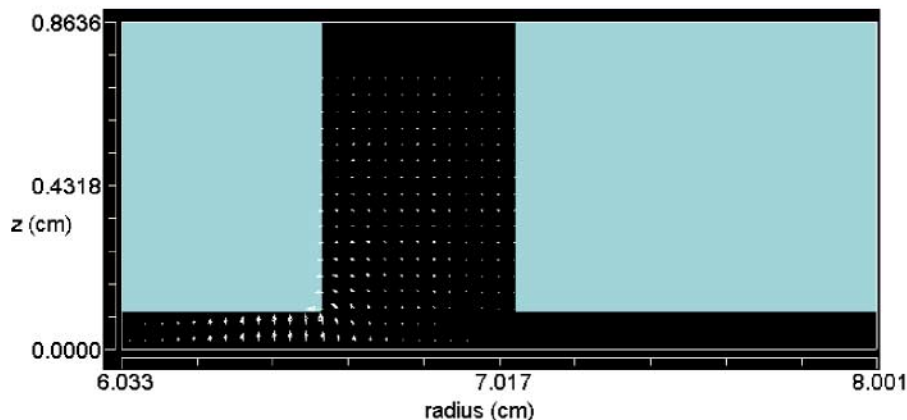


FIG. 19. (Color) MAFIA graphic showing electric field arrows for the WC475 choke resonance with azimuthal index 1. Note the axis orientation. The bottom edge of the plot is the symmetry plane at the gap center.

Imagine an arbitrarily long pillbox cavity of radius  $a$  resonating in the TE<sub>120</sub> mode; that is, at the TE<sub>12</sub> cutoff frequency. The TE<sub>12</sub> fields at cutoff are given by

$$H_\rho = H_\phi = E_z = 0, \quad E_\rho = \frac{Z_0}{k_c \rho} J_1(k_c \rho) \sin \phi, \quad H_z = J_1(k_c \rho) \cos \phi, \quad E_\phi = Z_0 J_1'(k_c \rho) \cos \phi, \quad (8)$$

where  $k_c = \chi_{12}/a = p'_{12}/a$ . For a small perturbation of the wall which places it at  $\rho(\phi) = a + a_2 \cos 2\phi$ , we calculate the fractional change in resonant frequency or cutoff wave number as follows:

$$\begin{aligned} \frac{\Delta k_c}{k_c} &= \frac{\int_{\Delta A} (\epsilon_0 |\mathbf{E}|^2 - \mu_0 |\mathbf{H}|^2) dA}{\int_A (\epsilon_0 |\mathbf{E}|^2 + \mu_0 |\mathbf{H}|^2) dA} \approx \frac{\int_0^{2\pi} [\epsilon_0 |\mathbf{E}(a, \phi)|^2 - \mu_0 |\mathbf{H}(a, \phi)|^2] a_2 \cos 2\phi d\phi}{\int_0^{2\pi} \int_0^a (\epsilon_0 |\mathbf{E}|^2 + \mu_0 |\mathbf{H}|^2) \rho d\rho d\phi} \\ &= \frac{-\frac{\pi}{2} \mu_0 a a_2 (1 + 1/p'_{12}) J_1^2(p'_{12})}{\mu_0 \pi \frac{a^2}{p'_{12}} [\int_0^{p'_{12}} \frac{1}{x} J_1^2(x) dx + \int_0^{p'_{12}} x J_1^2(x) dx + \int_0^{p'_{12}} x J_1^2(x) dx]} \\ &= -0.5365 \frac{a_2}{a}. \end{aligned} \quad (9)$$

Now, the splitting in guide wave number at our operating frequency is obtained from

$$\Delta\beta = \sqrt{k_0^2 - k_c^2(1 - \Delta k_c/k_c)^2} - \sqrt{k_0^2 - k_c^2(1 + \Delta k_c/k_c)^2}. \quad (10)$$

For  $k_0 = 239.43 \text{ m}^{-1}$  ( $f = 11.424 \text{ GHz}$ ) and  $a = 0.060325 \text{ m}$  ( $d = 4.75 \text{ in.}$ ), a wall deformation of  $0.254 \text{ mm}$  ( $0.010 \text{ in.}$ ) gives  $\Delta\beta = 0.1586 \text{ m}^{-1}$ . If this deformation is continuous and at  $45^\circ$  to the incoming polarization direction, it will produce a circular polarization (half the power lost to the cross polarization) in just under  $10 \text{ m}$  and a  $90^\circ$  mode rotation (all power lost to the cross polarization) in  $19.81 \text{ m}$ . Although this assumes the worst case scenario for orientation and coherence, we cannot expect tolerances much better than this for such waveguide. For the prospect of accurately preserving polarization over  $50$  or a  $100 \text{ m}$ , this calculation does not bode well.

## 2. Correcting for polarization mixing

In general, coupling between the two polarizations of TE<sub>12</sub> over a long distance due to random waveguide imperfections will not result in a simple polarization rotation, but in an elliptical polarization. That is, there can be an arbitrary relative amplitude between the two orthogonal components and an arbitrary relative phase. We can show, however, that for a length of circular waveguide with small, smoothly varying, elliptical deformations there exists an orientation at which a polarized mode can be launched such that, despite mixing with its cross polarization, a pure linear polarization, at some angle, is transmitted to the other end of the guide.

We assume reflections and coupling to nondegenerate modes are negligible, so that we have only mode mixing between the two cross polarizations. We also assume that any difference in attenuation constants introduced by the deformations has a negligible effect. The general form for the mode-mixing matrix is then

$$\begin{aligned} \mathbf{M} &= e^{-\tau} \begin{bmatrix} \sqrt{1 - \alpha^2} e^{i\theta_1} & -\alpha e^{i(\theta_2 - \phi)} \\ \alpha e^{i(\theta_1 + \phi)} & \sqrt{1 - \alpha^2} e^{i\theta_2} \end{bmatrix} \\ &= e^{-\tau + i\theta} \begin{bmatrix} \sqrt{1 - \alpha^2} & -\alpha e^{i(\Delta\theta - \phi)} \\ \alpha e^{i\phi} & \sqrt{1 - \alpha^2} e^{i\Delta\theta} \end{bmatrix}, \end{aligned} \quad (11)$$

relating the amplitudes at the end to those at the beginning by

$$\mathbf{V}_2 = \mathbf{M}\mathbf{V}_1. \quad (12)$$

$\mathbf{M}$  is the lower left quadrant of the  $4 \times 4$  scattering matrix, or the transpose of the upper right, the other quadrants being zeros. Note that, if the axes are rotated  $90^\circ$ , the polarizations are switched and the phase length difference  $\Delta\theta$  for the transmitted components (diagonal elements) reverses sign. It follows that at some intermediate angle  $\Delta\theta$  is zero. Let us take this as our reference orientation, determined by the waveguide. In this basis, the mixing matrix simplifies to the form

$$\begin{aligned} \mathbf{M}_0 &= e^{-\tau + i\theta} \begin{bmatrix} \sqrt{1 - \alpha_0^2} & -\alpha_0 e^{-i\theta_0} \\ \alpha_0 e^{i\theta_0} & \sqrt{1 - \alpha_0^2} \end{bmatrix}, \\ \mathbf{V}_{20} &= \mathbf{M}_0 \mathbf{V}_{10}. \end{aligned} \quad (13)$$

We hope to find an angle for our mode decomposition axes for which, if we launch a single polarization, the wave at the end will also be linearly polarized, though not necessarily along the same axis. The rotation matrix for an angle  $\gamma$  is

$$\mathbf{R} = \begin{bmatrix} \cos \gamma & -\sin \gamma \\ \sin \gamma & \cos \gamma \end{bmatrix}, \quad (14)$$

and the modes in this basis are related to the reference modes as follows:

$$\begin{aligned} \mathbf{V}' &= \mathbf{R}\mathbf{V}_0, \\ \mathbf{V}'_2 &= \mathbf{R}\mathbf{V}_{20} = \mathbf{R}\mathbf{M}_0\mathbf{V}_{10} = \mathbf{R}\mathbf{M}\mathbf{R}^{-1}\mathbf{V}'_1 = \mathbf{M}'\mathbf{V}'_1. \end{aligned} \quad (15)$$

$$\begin{aligned}
\mathbf{M}' &= \mathbf{R}\mathbf{M}_0\mathbf{R}^{-1} \\
&= \begin{bmatrix} \cos\gamma & -\sin\gamma \\ \sin\gamma & \cos\gamma \end{bmatrix} e^{-\tau+i\Theta} \begin{bmatrix} \sqrt{1-\alpha_0^2} & -\alpha_0 e^{-i\phi_0} \\ \alpha_0 e^{i\phi_0} & \sqrt{1-\alpha_0^2} \end{bmatrix} \begin{bmatrix} \cos\gamma & \sin\gamma \\ -\sin\gamma & \cos\gamma \end{bmatrix} \\
&= \begin{bmatrix} \sqrt{1-\alpha_0^2} - 2i\alpha_0 \sin\phi_0 \sin\gamma \cos\gamma & -\alpha_0(e^{-i\phi_0} \cos^2\gamma + e^{i\phi_0} \sin^2\gamma) \\ \alpha_0(e^{-i\phi_0} \sin^2\gamma + e^{i\phi_0} \cos^2\gamma) & \sqrt{1-\alpha_0^2} + 2i\alpha_0 \sin\phi_0 \sin\gamma \cos\gamma \end{bmatrix}. \tag{16}
\end{aligned}$$

Now, a wave is linearly polarized if its two components in any Cartesian basis have the same phase. Thus, launching the first mode in our primed frame will give us what we want if, and only if, the complex phases of  $\mathbf{M}'_{11}$  and  $\mathbf{M}'_{21}$  are equal.

$$\begin{aligned}
\tan(\arg\mathbf{M}'_{11} - \Theta) &= -\frac{2\alpha_0 \sin\phi_0 \sin\gamma \cos\gamma}{\sqrt{1-\alpha_0^2}} \\
&= -\frac{\alpha_0 \sin\phi_0}{\sqrt{1-\alpha_0^2}} \sin 2\gamma, \\
\tan(\arg\mathbf{M}'_{21} - \Theta) &= \frac{\sin\phi_0(\cos^2\gamma - \sin^2\gamma)}{\cos\phi_0} \\
&= \tan\phi_0 \cos 2\gamma. \tag{17}
\end{aligned}$$

The solution is

$$\begin{aligned}
\gamma &= \frac{1}{2} \tan^{-1} \left( -\frac{\sqrt{1-\alpha_0^2}}{\alpha_0 \cos\phi_0} \right) \\
&= \frac{1}{2} \tan^{-1} \left[ \frac{-|\mathbf{M}_{011}|^2}{\text{Re}(\mathbf{M}_{011}\mathbf{M}_{021}^*)} \right]. \tag{18}
\end{aligned}$$

By scattering matrix unitarity, we conclude that launching the second primed polarization yields the orthogonal linear polarization at the end, although the final phases may differ. This can be verified by equating the phases of  $\mathbf{M}'_{12}$  and  $\mathbf{M}'_{22}$  and getting the same  $\gamma$ . In fact, the phases of the transmitted modes are oppositely displaced from  $\Theta$ .

Note that, as the coupled amplitude  $\alpha_0$  goes to zero, the angle  $\gamma$  goes to  $-\pi/4$ . This is because, for perfect elliptical guide, the symmetric orientation ( $\Delta\theta = 0$ ) is rotated  $\pi/4$  from the decoupled orientation.

### 3. Polarization rotator

We showed that, if we can choose both the launching orientation and the extraction orientation, we should be able to arrange for optimal transmission of the polarized mode power. Since launchers and extractors will be fixed by the mechanical layout, and the waveguide itself will be too long to rotate in place, what we require is a device at the start and end of each run which can rotate the mode through an arbitrary angle without introducing any circular polarization or coupling to other modes.

A 90° rotator placed at the proper orientation can give a rotation of any desired angle. The cross section of the rotator deviates from circular in such a way that the eigenmodes corresponding to TE<sub>12</sub> polarizations have phase lengths through the device which differ by  $\pi$ . Components of an incoming wave projected along the rotator's axes thus acquire a relative sign difference. The effect is to rotate the polarization direction by twice the angle between the incoming orientation and the rotator axes. One can easily convince oneself of this graphically or by considering the following: Take a horizontally polarized wave passing through such a polarization rotator whose eigenmode axes (primed frame) are oriented at an angle  $\psi$ . The polarization vector transforms as follows:

$$\begin{aligned}
\mathbf{V}_{\text{in}} &= \hat{x} = \cos\psi \hat{x}' - \sin\psi \hat{y}' \\
\mathbf{V}_{\text{out}} &= e^{i\theta} V_{\text{in},x'} \hat{x}' + e^{i(\theta+\pi)} V_{\text{in},y'} \hat{y}' = e^{i\theta} (V_{\text{in},x'} \hat{x}' - V_{\text{in},y'} \hat{y}') = e^{i\theta} (\cos\psi \hat{x}' + \sin\psi \hat{y}') \\
&= e^{i\theta} [\cos\psi (\cos\psi \hat{x} + \sin\psi \hat{y}) + \sin\psi (-\sin\psi \hat{x} + \cos\psi \hat{y})] = e^{i\theta} (\cos 2\psi \hat{x} + \sin 2\psi \hat{y}). \tag{19}
\end{aligned}$$

The polarization has been rotated by  $2\psi$ .

In designing a rotator in overmoded waveguide, one needs to consider coupling to parasitic modes as well, especially since it is desirable to use a relatively large deformation to keep the device compact. The problem must therefore be treated as a mode coupling problem rather than simply a phase length problem. The amplitudes of involved propagating modes along the rotator are determined by simultaneously integrating a set of coupling equations.

For a general wall deformation expressed as  $r(\phi, z) = a + \delta(\phi, z)$ , with

$$\delta(\phi, z) = a_0^c(z) + \sum_{l=1}^{\infty} [a_l^c(z) \cos l\phi + a_l^s(z) \sin l\phi], \tag{20}$$

the first-order coupling equations for the mode amplitudes, with the propagation constants factored out, take the general form

$$\begin{aligned} \frac{d}{dz} A_m^o(z) &= \sum_n \{ [K_{mnc}^{oo} a_{p-q}^c(z) + C_{mnc}^{oo} a_{p+q}^c(z)] A_n^o(z) \\ &\quad + [K_{mns}^{ox} a_{p-q}^s(z) + C_{mns}^{ox} a_{p+q}^s(z)] A_n^x(z) \} e^{\Delta\Gamma_{mn}z}, \\ \frac{d}{dz} A_m^x(z) &= \sum_n \{ [K_{mns}^{xo} a_{p-q}^s(z) + C_{mns}^{xo} a_{p+q}^s(z)] A_n^o(z) \\ &\quad + [K_{mnc}^{xx} a_{p-q}^c(z) + C_{mnc}^{xx} a_{p+q}^c(z)] A_n^x(z) \} e^{\Delta\Gamma_{mn}z}. \end{aligned} \quad (21)$$

The subscripts  $m$  and  $n$  each signify a fully characterized mode (except for polarization), with indices  $ph$  and  $qk$ , respectively.  $\Delta\Gamma_{mn} = (\alpha_m - \alpha_n) + j(\beta_m - \beta_n)$  is the difference in propagation constants, and the sums are over all propagating modes. For modes with a nonzero first index, an  $o$  superscript indicates the ordinary polarization, and an  $x$  superscript indicates the cross polarized mode. Of course, when  $p$  or  $q = 0$ , there is only one mode  $m$  or  $n$ . TE<sub>0n</sub> modes are here considered ordinary polarizations, and TE<sub>0n</sub> modes are grouped with the cross polarizations. A perturbation  $a_l$  couples modes the sum or difference of whose first indices is  $l$ . The  $K$ 's provide the coupling between pairs of modes with the latter relationship and the

$C$ 's between those with the former. The cosinelike deformations,  $a_l^c$ , are used when  $m$  and  $n$  are both ordinary or are both cross polarized modes, while the sinelike deformations,  $a_l^s$ , couple between the two sets.

The coupling coefficients are given by Doane [17]. We collect his results here, with minor changes in notation. A general coefficient  $\kappa_{mn}$  is calculated between pairs of modes from

$$\kappa_{mn} = \frac{-j}{2a^3} \frac{\varepsilon_{p-q} T_{mn}}{\sqrt{\beta_m \beta_n} (\beta_m + \beta_n)}, \quad \varepsilon_l = \begin{cases} 2, & l = 0, \\ 1, & l \neq 0, \end{cases} \quad (22)$$

and

$$\begin{aligned} T_{mn} &= \text{sgn}(q) \sqrt{\frac{\varepsilon_q}{\varepsilon_p}} \frac{\beta_m \chi_n^2 (\chi_m^2 - pq) + \beta_n (\chi_n^2 - pq)}{\sqrt{(\chi_m^2 - p^2)(\chi_n^2 - q^2)}}, & \text{TE}_{ph} - \text{TE}_{qk}, & \quad p \geq q, \\ T_{mn} &= \sqrt{\frac{\varepsilon_q}{\varepsilon_p}} (\beta_m \chi_n^2 + \beta_n \chi_m^2), & \text{TM}_{ph} - \text{TM}_{qk}, & \quad p \geq q, \\ T_{mn} &= \frac{\sqrt{\varepsilon_q} k_0 (\chi_m^2 - \chi_n^2) p}{\sqrt{\chi_m^2 - p^2}}, & \text{TE}_{ph} - \text{TM}_{qk}. & \end{aligned} \quad (23)$$

The factors in our differential equations are then governed by the following rules:

$$\begin{aligned} D_{mnc}^{rr} &\equiv 0, \\ D_{nmw}^{tr} &= D_{mnw}^{rt}, \\ p = q : &\begin{cases} K_{mnc}^{oo} = K_{mnc}^{xx} = \kappa_{mn}, & p = q \neq 0, \\ K_{mnc}^{oo} = K_{mnc}^{xx} = (-1)^{h-k} \kappa_{mn}, & p = q = 0, \\ K_{mns}^{ox} = K_{mns}^{xo} = 0, \end{cases} \\ p \neq |q| : &\begin{cases} K_{mnc}^{oo} = K_{mnc}^{xx} = K_{mns}^{ox} = -K_{mns}^{xo} = \kappa_{mn}, & q \neq 0, \\ K_{mnc}^{oo} = K_{mns}^{xo} = (-1)^k \kappa_{mn}, & q = 0 \text{ (TE}_{0k}\text{)}, \\ K_{mnc}^{xx} = -K_{mns}^{ox} = (-1)^{k+1} \kappa_{mn}, & q = 0 \text{ (TM}_{0k}\text{)}, \end{cases} \quad (24) \\ C_{mnw}^{rt} &\equiv 0, \quad q = 0, \\ C_{mns}^{ox} &= C_{mns}^{xo} = \kappa_{mn}(q \rightarrow -q), \quad q \neq 0, \\ C_{mnc}^{oo} &= -C_{mnc}^{xx} = -\kappa_{mn}(q \rightarrow -q), \quad q \neq 0, \end{aligned}$$

where  $D = K$  or  $C$ ,  $r$  and  $t = o$  or  $x$ , and  $w = c$  or  $s$ . Note that, for the  $C$ 's,  $\kappa_{mn}$  must be calculated using  $-q$  instead of  $q$  [hence the  $\text{sgn}(q)$  in Eq. (23)]. For completeness, we note that coupling to backward waves is ignored in this treatment, as it is assumed negligible for gentle wall variations.

Since  $a_0^s \equiv 0$ , the two TE<sub>12</sub> polarizations are directly coupled only by  $a_2^s(z)$  through  $C_{mns}^{xo} = C_{mms}^{xo}$ . To preserve a linear polarization, we must design our device to rotate by 90°, or completely transfer power between the two polarizations. To first order, ignoring the effect of other modes, this requires

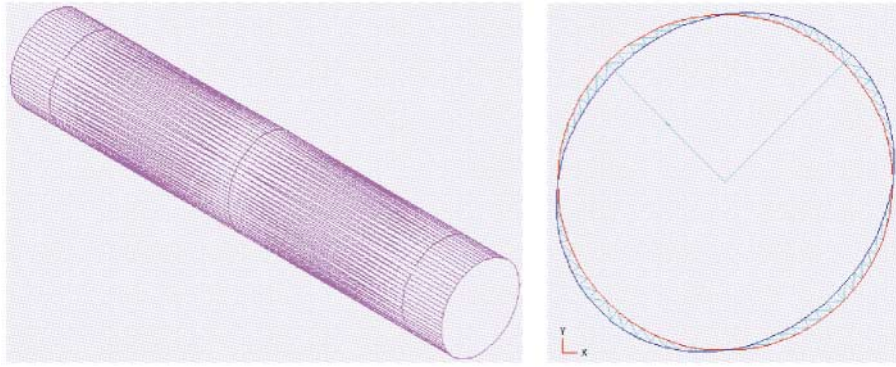


FIG. 20. (Color) Mode rotator geometry and cross section. The two tapers total 22.86 cm. The superposition of the circular cross section of the ends (red) and the central cross section (blue) shows the maximum deformation of 6.8%.

$$\int_0^L |C_{[12][12]_s}^{ox}| a_2^s(z) dz = \frac{\pi}{2}. \quad (25)$$

As a check on our earlier perturbation calculation, one can calculate for 12.065 cm diameter waveguide at 11.424 GHz the  $TE_{12}$  polarization coupling  $C_{[12][12]_s}^{ox} = j312.1 \text{ m}^{-2}$  and verify that, for a constant  $a_2^s = 0.254 \text{ mm}$ , the above condition requires  $L = 19.81 \text{ m}$ .

The polarization rotator we designed and built is in 5.08 cm diameter waveguide. To avoid reflections and minimize unwanted coupling, we adiabatically introduce and remove a wall perturbation characterized by

$$f(z, \phi) = a + a_2^s(z) \sin 2\phi. \quad (26)$$

For manufacturability by wire EDM, we let  $a_2^s(z)$  taper in and out linearly over 11.43 cm each way to a maximum displacement of  $a_{2\text{max}}^s = 1.73 \text{ mm}$ , yielding a total active length of 22.86 cm. The geometry is illustrated in Fig. 20. Figure 21 shows the mode amplitudes along the rotator. The dominant parasitic mode,  $TE_{31}$ , carries a couple of percent of the power in each of its polarizations

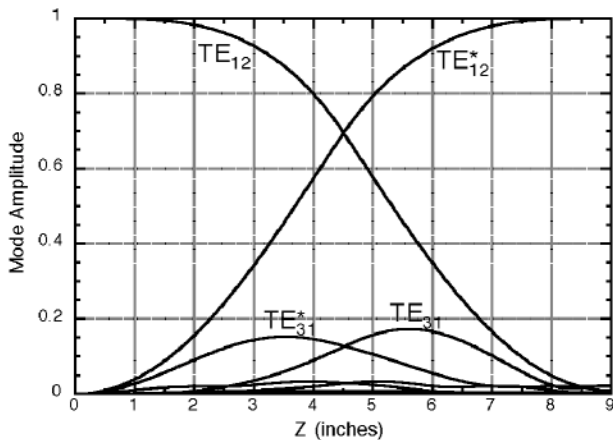


FIG. 21. Calculated mode amplitude profiles along the polarization converter, or mode rotator, for an entering  $TE_{12}$  wave. The asterisks here indicate cross-polarized modes.

near the center of the device, but this mostly beats back into the desired mode by the end.  $TE_{11}$  and  $TM_{11}$  enter at lower levels ( $TE_{31}$  is cut off). The simulated efficiency is about 99.9%. The design was checked, in terms of the phase length difference in the uncoupled orientation, with the field solver HP-HFSS [13]. A second design, which also preserves  $TE_{01}$  purity, is 43.50 cm long with linear tapers and a central straight section, all of equal length, and  $a_{2\text{max}}^s = 0.66 \text{ mm}$ .

#### IV. TRANSPORT LINE MEASUREMENTS

Measurements of three types were performed on the 55 m circular waveguide. First, the modal structure at the end of the waveguide was measured using the mode analyzer while launching the  $TE_{01}$  and  $TE_{12}$  modes. Second, we measured the transmission attenuation of the guide by putting a mode transducer at each end of the waveguide. This was done for both  $TE_{01}$  and  $TE_{12}$  modes. Finally, we measured the round-trip attenuation by placing a short circuit at the input of the mode launcher at one end of the waveguide while measuring the reflection coefficient at the other end.

For the last two types of measurement there are two mode converters, one at each end of the waveguide. For other than the intended mode, the transport line and mode converters act as a very big resonator with a huge number of resonances. Fortunately, the filling time of these resonances is longer than the pulse width of the signal intended to be sent through this line. However, all the measurements are made at steady state. Hence, they are cluttered with these resonances. The remedy is to collect data in phase and magnitude over a frequency range, and then synthesize the response of the system to a pulse. The pulse of choice has Gaussian rise and fall times and a flattop. This pulse has the advantage of a minimum bandwidth for a given rise time. Explicitly, the pulse has the following form:

$$p(t) = \begin{cases} e^{[(t+t_0)/\tau]^2}, & t < -t_0, \\ 1, & -t_0 < t < t_0, \\ e^{[(t-t_0)/\tau]^2}, & t > t_0. \end{cases} \quad (27)$$

The rise time  $t_r$  of this pulse, defined as the time spent for the pulse to rise from 0.1 to 0.9 of its final value, is given by

$$t_r = 1.19283\tau. \tag{28}$$

The pulse width,  $t_w$ , defined as the time between 3 dB points, is given by

$$t_w = 1.39593t_r + 2t_0. \tag{29}$$

Using Eqs. (28) and (29), one determines the coefficients  $\tau$  and  $t_0$  from the desired pulse width and rise time. In most cases, the pulse width of choice is 300 ns and the

rise time is 75 ns. The frequency domain measurements on the system were made with a bandwidth of 50 MHz, around 11.424 GHz. The number of points acquired in this bandwidth is 801 points.

### A. TE<sub>12</sub> mode measurements

The TE<sub>12</sub> mode transducer, combined with the arc taper, was used to launch the TE<sub>12</sub> mode into the 55 m transport line. The mode analyzer was installed at the other end and the mode spectrum was measured. The resulting spectrum is shown in Fig. 22. When comparing

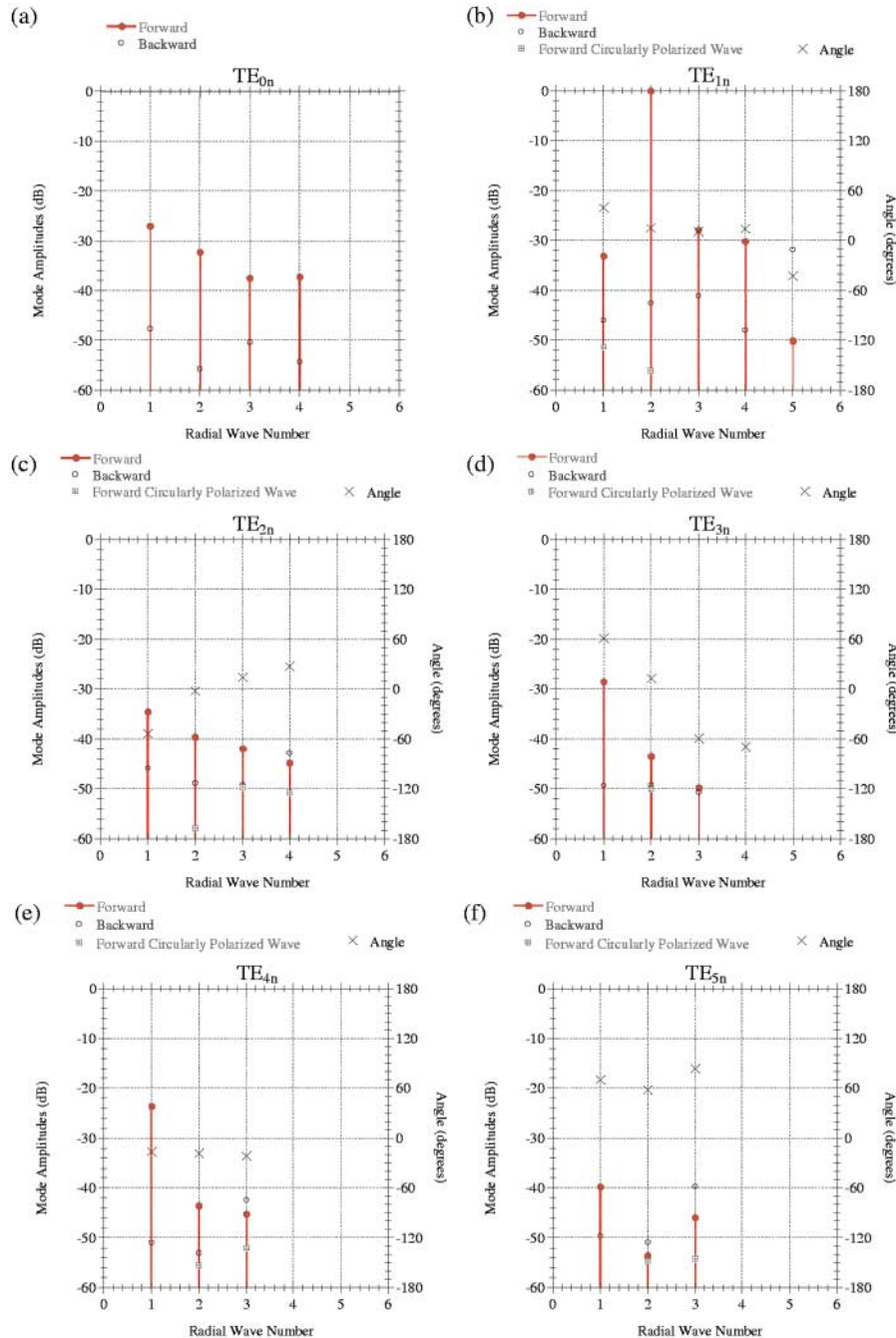


FIG. 22. (Color) The mode spectrum after the transport line when the injected signal is the TE<sub>12</sub> model.

Fig. 22 with Fig. 11, one can make the following observations.

(i) The angle of rotation of the  $TE_{12}$  mode before and after the transport line is almost the same. Furthermore, the level of the circularly polarized wave in both cases is very small. Hence, one can conclude that *there is no detectable cross polarization mode mixing*. This can be justified by assuming that the circular waveguide that comprises the transport line has a wall displacement with a very small second azimuthal harmonic.

(ii) In general, mode contamination in all modes has an elevated level after the transport line. However, this is most noticeable in the case of  $TE_{41}$ . The level of this mode has increased from  $-39$  to  $-23.5$  dB. This mode has the highest level of all parasitic modes after the transport line. It happens that the  $TE_{41}$  mode is virtually degenerate with the  $TE_{12}$  mode; the beat wavelength between those two modes is 72.89 m. This, combined with the fact that the coupling coefficient between  $TE_{12}$  and  $TE_{41}$  is greater than the cross polarization coupling coefficient [see Eq. (23)], indicates that the 3rd and 5th azimuthal harmonics in waveguide wall displacement play an important role in the transport of signals over the  $TE_{12}$  mode.

(iii) The level of the  $TE_{13}$  mode has dropped. It is smaller than the value measured without the transport line and smaller than the mode matching prediction for the mode analyzer. This could be justified with a very small amount of  $TE_{13}$  being generated in the transport line. Levels as low as  $-35$  dB, interfering out of phase with the contamination generated by the mode analyzer, could lead to this effect.

Since mode rotation was not a problem, there was no need to use the polarization rotator. Nonetheless, for

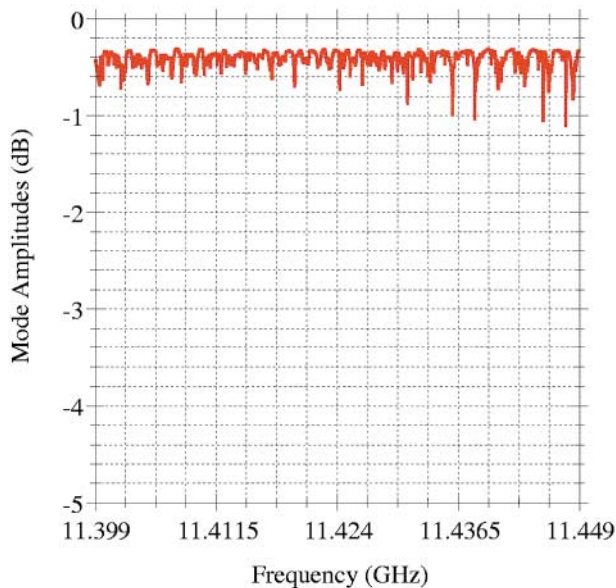


FIG. 23. (Color) Transmission through two  $TE_{12}$  mode transducers, two arc tapers, and 55 m of 12.065 cm diameter circular waveguide.

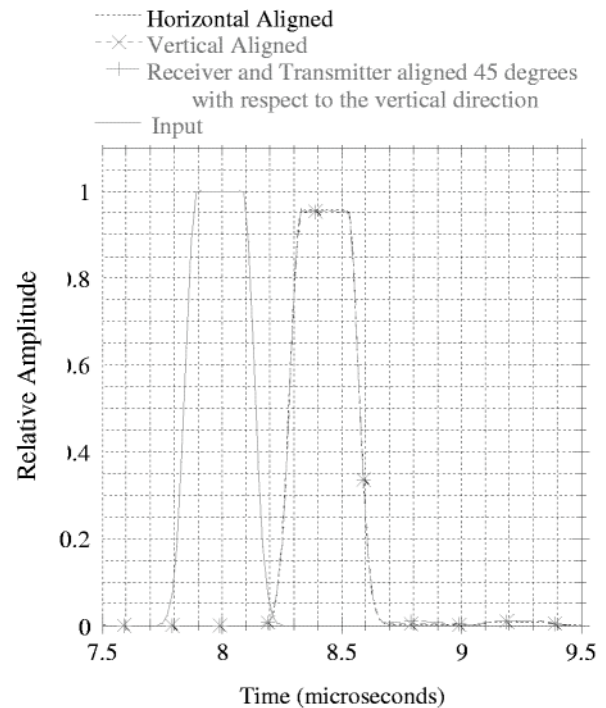


FIG. 24. Time domain response of the transport line plus the mode launchers (two mode transducers plus two arc tapers). For this figure, the two mode transducers were always aligned with respect to each other.

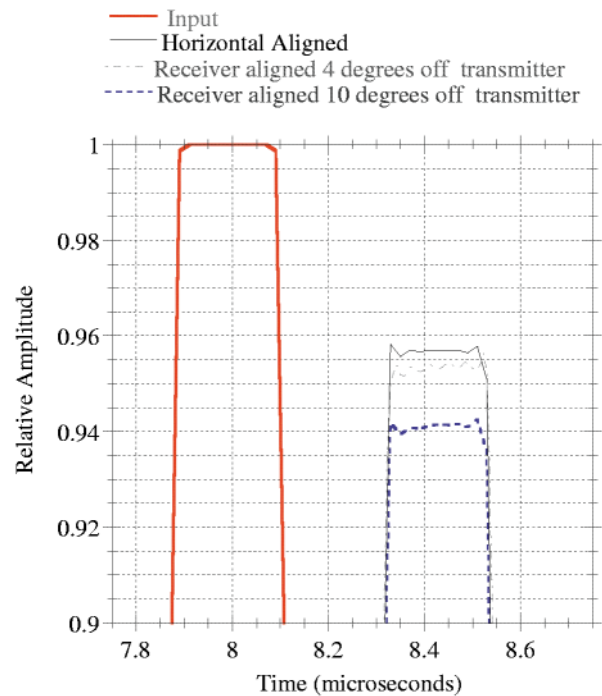


FIG. 25. (Color) The effect of rotating one of the mode  $TE_{12}$  mode transducers with respect to the other.

completeness, we installed the polarization rotator at the beginning of the transport line, rotated the mode transducer 90° to produce horizontal polarization, and then used the polarization rotator to bring it back to the vertical direction. The resulting modal spectrum was quite similar to that shown in Fig. 22.

To further evaluate the transport line transmission properties, we measured the total transmission through two mode launchers, two arc tapers, and the transport line. This is shown in Fig. 23. In this figure, the effect of the

rectangular waveguide, which is used to deliver the signal to the beginning of the line, is calibrated out (see Figs. 6 and 4). First, the measurements were done with the two mode transducers aligned in orientation. We varied, however, their angle with respect to the transport line (or the gravity vector). Figure 24 shows that the transmitted pulse did not depend on the common angle of rotation. Then, we varied the angle of one transducer with respect to the other. Figure 25 shows that the maximum signal was obtained only when the two mode transducers were perfectly

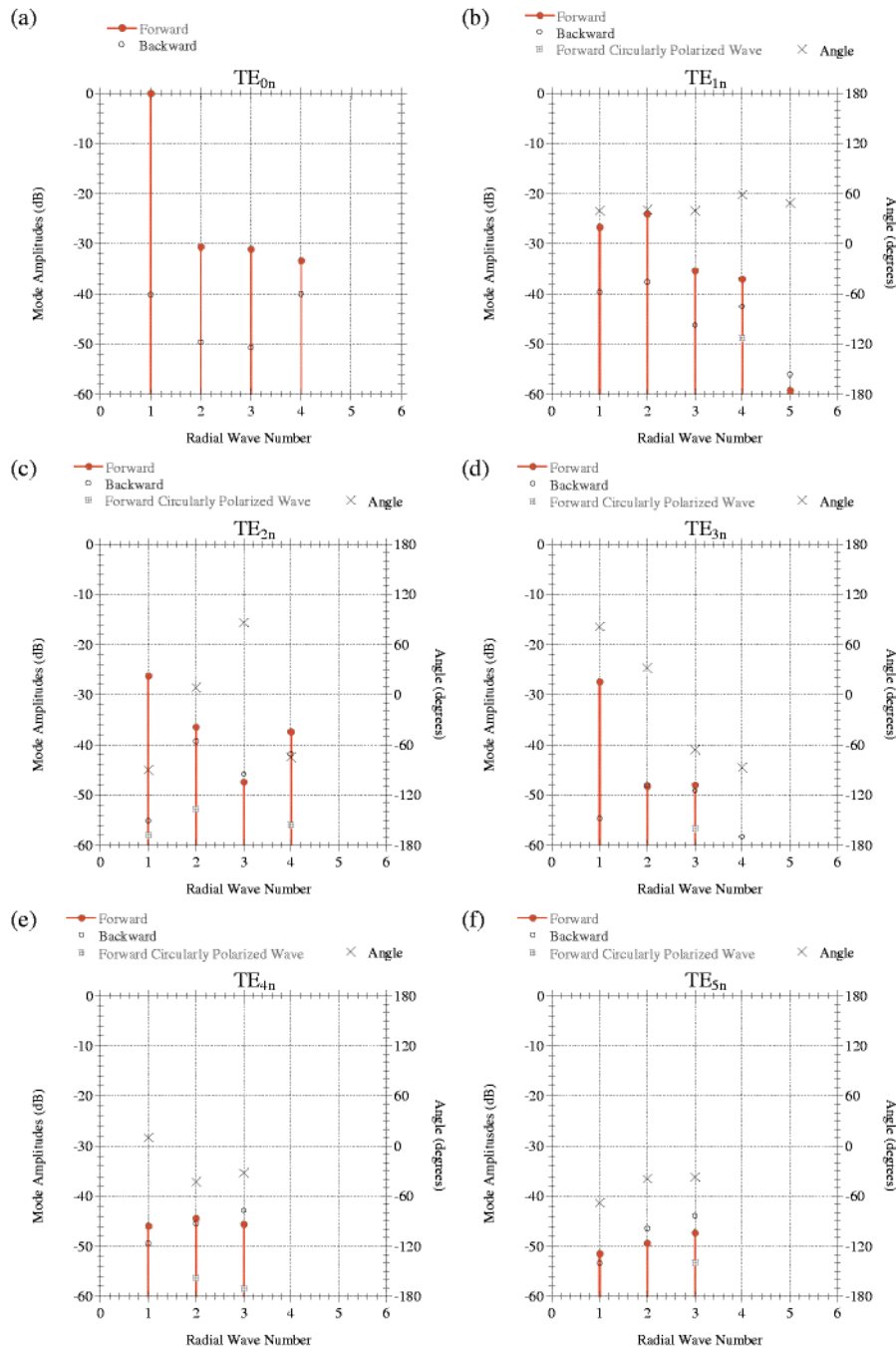


FIG. 26. (Color) The mode spectrum after the transport line when the injected signal is the TE<sub>01</sub> mode.

aligned. Again, from Figs. 24 and 25, one can reach only one conclusion: *there is no detectable cross polarization mode mixing.*

The overall level of the received signal is  $-0.38$  dB. Approximately 8.3% of the input power has been lost. This cannot be completely accounted for by the losses of the two mode transducers and the arc tapers (4.5%; see Fig. 10), the transmission line losses (theoretically 2.6%), plus mode conversion to  $TE_{41}$  mode (0.5%; see Fig. 22). It is conceivable that the extra loss (0.7%) is due to conversion to one or more TM modes.

### B. $TE_{01}$ mode measurements

We repeated the same type of measurements for the  $TE_{01}$  mode. The modal spectrum at the end of the line is shown in Fig. 26. In comparison with Fig. 15, one notices increased levels of both the  $TE_{21}$  and  $TE_{31}$  modes, though these levels remain below  $-25$  dB. There is also a substantial increase in the levels of the  $TE_{12}$  and  $TE_{11}$  modes. However, one should notice that these modes were present before inserting the transport line. Hence, if their presence then was due to the mode analyzer itself, any small generation of these modes through the transport line could conspire (add in phase) to produce these high levels in the mode analyzer.

The assumptions about the  $TE_{12}$  and  $TE_{11}$  modes seem to be confirmed by the transmission measurements shown in Fig. 27 and the associated time domain measurements shown in Fig. 28. These show a total loss through the mode transducers, arc tapers, and transport line of about 3%. The mode transducers and the tapers account for 2% of these losses, and the theoretical transport line losses for

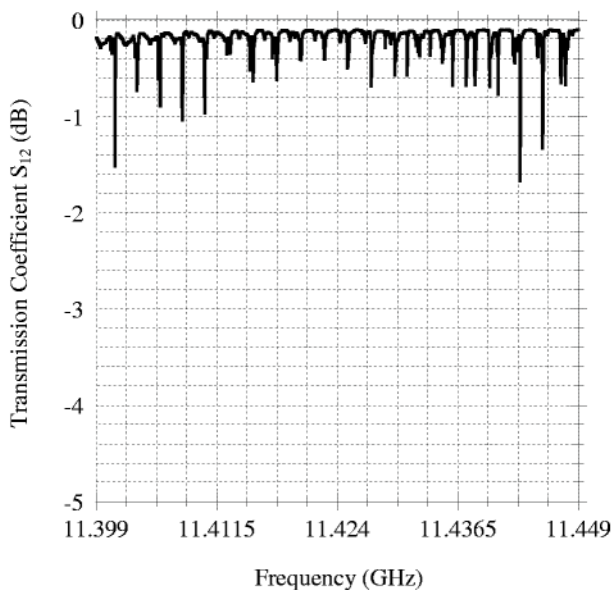


FIG. 27. Transmission through two  $TE_{01}$  mode transducers, two arc tapers, and 55 m of 12.065 cm diameter circular waveguide.

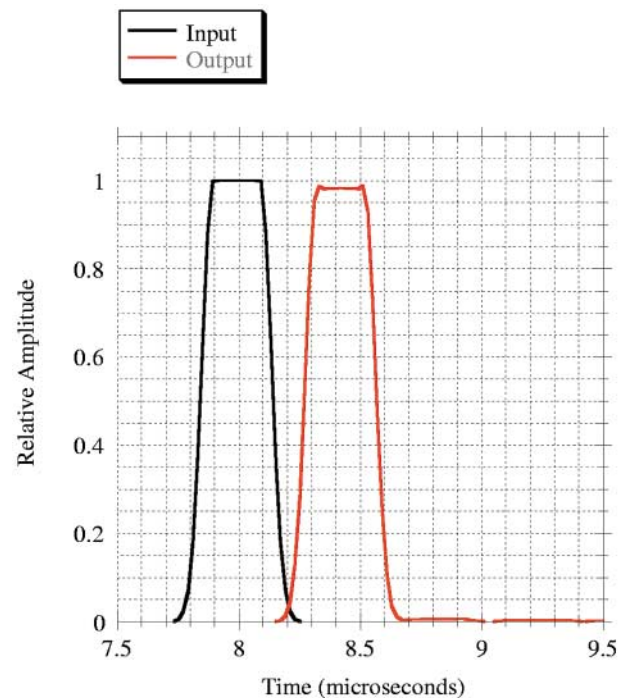


FIG. 28. (Color) Time domain response of the transport line plus the mode launchers (two  $TE_{01}$  mode transducers plus two arc tapers).

this mode are 1%. This measurement confirms that, at least, our assumption for Ohmic losses is correct.

### V. CONCLUSION

We demonstrated the possibility of using the  $TE_{12}$  mode in highly overmoded circular waveguides as a means of low-loss transport of rf power. The overall losses were small and compared relatively well with theory. The waveguide used in the experiments was extruded, oxygen-free, high-conductivity copper. It was shown that this waveguide could be manufactured well enough to avoid noticeable cross-polarization mode mixing. Nonetheless, we observed some conversion to the virtually degenerate mode  $TE_{41}$ . However, the conversion levels were small.

We also compared our results for  $TE_{12}$  with those of the low loss  $TE_{01}$ . In this process we showed that connecting flanges and waveguides could be used to propagate either mode. This paves the way to develop a multimoded system in which different signals are loaded over different modes.

We reported a novel technique for measuring the modal content of a highly overmoded waveguide. We also reported techniques for efficiently exciting the  $TE_{12}$  mode and  $TE_{01}$  modes. Finally, we showed how to design and implement a polarization rotator for the  $TE_{12}$  mode.

### ACKNOWLEDGMENTS

We thank R. J. Loewen for writing most of the data acquisition and control systems codes. We thank R. D. Ruth, P. B. Wilson, Z. D. Farkas, R. H. Miller, D. L. Burke, and

C. Adolphsen for many useful discussions and for their continual support of this work. We thank the manufacturing and mechanical designers at SLAC for their continual support and help. The help of the ATF Group and workers at KEK was an indispensable part of this work. We also thank R. L. Ives, W. Lawson, B. Hogan, and the Calabazas Creek team for many useful discussions and for their prompt help and continual support. This work was supported by the U.S. Department of Energy Contract No. DE-AC03-76SF00515, the DOE SBIR Project (Calabazas Creek, Inc.), and by KEK, Japan.

- 
- [1] S. G. Tantawi *et al.*, in *Advanced Accelerator Concepts: Eighth Workshop*, edited by Wes Lawson, AIP Conf. Proc. No. 472 (AIP, New York, 1999), pp. 967–974.
- [2] The NLC Design Group, Report No. LBNL-PUB-5424, SLAC Report No. 474, and Report No. UCRL-ID 124161, 1996.
- [3] The JLC Design Group, KEK-REPORT-97-1, 1997.
- [4] Z. D. Farkas, *IEEE Trans. Microwave Theory Tech.* **34**, 1036–1043 (1986).
- [5] P. B. Wilson, Z. D. Farkas, and R. D. Ruth, in *Proceedings of the Linear Accelerator Conference, Albuquerque, NM, 1990* (Report No. SLAC-PUB-5530, 1990).
- [6] H. Mizuno and Y. Otake, in *Proceedings of the 17th International Linac Conference (LINAC 94), Tsukuba, Japan, 1994* (KEK, Ibaraki, Japan, 1994).
- [7] S. G. Tantawi, R. D. Ruth, and P. B. Wilson, in *Proceedings of the IEEE Particle Accelerator Conference, New York, 1999* (IEEE, Piscataway, NJ, 1999), pp. 423–425.
- [8] Z. D. Farkas *et al.*, in *Proceedings of the 1993 Particle Accelerator Conference (PAC93), Washington, DC* (Report No. SLAC-PUB-6100, 1993).
- [9] Sami G. Tantawi *et al.*, *IEEE Trans. Microwave Theory Tech.* **47**, 2539–2546 (1999); Report No. SLAC-PUB-8074, 1999.
- [10] GORE-TEX cable assembly, part No. FBOHD0HD072.0.
- [11] LabVIEW5.1, Copyright 1999 National Instruments.
- [12] H. Hayano, in *Proceedings of the 18th International Linac Conference (LINAC 96), Geneva, 1996* (CERN, Geneva, 1996), pp. 547–551.
- [13] HP High Frequency Structure Simulator, Version 5.4, Copyright 1996–1999 Hewlett-Packard Co.
- [14] E. Luneville, J. Krieg, and E. Giguët, *IEEE Trans. Microwave Theory Tech.* **46**, 1–9 (1998).
- [15] J. L. Doane, *Int. J. Infrared Millim. Waves* **5**, 737–751 (1983).
- [16] MAFIA User's Guide Version 4.00, CST GmbH, Lauteschlaegerstr. 38, 64285 Darmstadt, Germany.
- [17] J. L. Doane, *Int. J. Electron.* **61**, 1109–1133 (1986).